

# $\tau$ Lepton Reconstruction at FCC-ee

Bachelor's Thesis of

Lars Bogner

At the KIT Department of Physics  
Institute of Experimental Particle Physics

First examiner: Prof. Markus Klute

Second examiner: Dr. Xunwu Zuo

First advisor: Dr. Xunwu Zuo

Second advisor: Dr. Jan Kieseler

Third advisor: Sofia Giappichini

24. April 2024 – 22. July 2024

ETP-BACHELOR-KA/2024-10

Karlsruher Institut für Technologie  
Institut für Experimentelle Teilchenphysik  
Postfach 6980  
76128 Karlsruhe

---

I declare that I have developed and written the enclosed thesis completely by myself. I have not used any other than the aids that I have mentioned. I have marked all parts of the thesis that I have included from referenced literature, either in their original wording or paraphrasing their contents. I have followed the by-laws to implement scientific integrity at KIT.

Ich versichere wahrheitsgemäß, die Arbeit selbstständig verfasst, alle benutzten Quellen und Hilfsmittel vollständig und genau angegeben und alles kenntlich gemacht zu haben, was aus Arbeiten anderer unverändert oder mit Abänderungen entnommen wurde sowie die Satzung des KIT zur Sicherung guter wissenschaftlicher Praxis in der jeweils gültigen Fassung beachtet zu haben.

**Karlsruhe, July 22, 2024**

.....  
(Lars Bogner)





# Abstract

The next generation of  $e^+e^-$ -colliders, such as the proposed Future Circular Collider electron-positron (FCC-ee) at CERN operating as a Higgs and electroweak factory, necessitates new implementations while enabling innovative approaches in  $\tau$  lepton reconstruction. In the FCC dataset, the  $\tau$  lepton plays a crucial role in many physics topics. Focusing on the IDEA detector concept at the FCC-ee, machine learning (ML) approaches for jet flavor tagging are studied. Additionally, explicit reconstruction algorithms are employed for tagging the decay mode of  $\tau$  leptons from its decay products on the jet level.

In the study about using ML for identifying the flavor of  $Z$  boson decay jets, the existing, state-of-the-art Particle Transformer Network shows very good performance with very low false positive rates in quark jet suppression against  $Z \rightarrow \tau^+\tau^-$  signal samples. A more simplistic feed-forward neural network is compared against the transformer model and shows worse performance with an increased false positive rate of two orders of magnitude.

Using an explicit reconstruction approach for the  $\tau$  decay mode identification, the combination with the reconstruction of intermediate states, like the neutral  $\pi^0$  meson or the  $\rho(770)^\pm$  meson is proposed. The performance of this method is evaluated in dependence on multiple cuts on the jet properties, aiming at optimizing the purity of the identified decay modes and investigating the efficiency-purity-relation.

The proposed techniques promise good performance in  $\tau$  reconstruction at FCC-ee but also further the need for a full simulation of the Innovative Detector for Electron-positron Accelerator (IDEA) detector to find final conclusions on the limitations of  $\tau$  lepton reconstruction, as the current fast simulation shows limitations for the reconstruction of  $\tau$  leptons. Additionally, alternative approaches to the tasks at hand are proposed.



# Zusammenfassung

Die nächste Generation von  $e^+e^-$ -Collidern, wie der am CERN geplante FCC-ee, der als „Higgs-Fabrik“ und „elektroschwache Fabrik“ arbeitet, erfordert neue Implementierungen und ermöglicht gleichzeitig innovative Ansätze bei der Rekonstruktion des  $\tau$ -Leptons. Im FCC-Datensatz spielt das  $\tau$ -Lepton für viele physikalische Fragestellungen eine entscheidende Rolle. Mit Schwerpunkt auf dem IDEA-Detektorkonzept am FCC-ee werden ML-Ansätze für Jet Flavor Tagging untersucht. Zusätzlich werden explizite Rekonstruktionsalgorithmen verwendet, um den Zerfallsmodus von  $\tau$ -Leptonen aus ihren Zerfallsprodukten auf Jet-Ebene zu bestimmen.

Beginnend mit der Verwendung von ML zur Identifizierung des Flavors von Z-Boson-Zerfallsjets zeigt das dem aktuellen Stand der ML-Technik entsprechende Particle Transformer Network eine herausragende Leistung mit sehr niedrigen False-Positive-Raten bei der Unterdrückung von Quarkjets im Vergleich zu Jets aus dem Zerfall  $Z \rightarrow \tau^+\tau^-$ . Ein einfacheres neuronales Feed-Forward-Netzwerk wird mit dem Transformer-Modell verglichen und zeigt eine schlechtere Leistung mit einer False-Positive-Rate, die um zwei Größenordnungen höher ist.

Unter Anwendung eines expliziten Rekonstruktionsansatzes zur Identifizierung der  $\tau$ -Zerfallsmoden wird eine Kombination mit Rekonstruktion von Zwischenzuständen, wie dem neutralen  $\pi^0$ -Meson oder dem  $\rho(770)^\pm$ -Meson, vorgeschlagen. Die Performance dieser Methode wird in Abhängigkeit von mehreren Einschränkungen der Jeteigenschaften bewertet, mit dem Ziel, die Reinheit der identifizierten Zerfallsmoden zu optimieren und die Effizienz-Reinheits-Beziehung zu untersuchen.

Die vorgestellten Techniken lassen eine gute Leistung bei der  $\tau$ -Rekonstruktion am FCC-ee erwarten, zeigen aber auch, dass eine vollständige Simulation des IDEA-Detektors notwendig ist, um endgültige Schlüsse über die Grenzen der  $\tau$ -Lepton-Rekonstruktion ziehen zu können, da die derzeitige schnelle Simulation, Grenzen für die Rekonstruktion von  $\tau$ -Leptonen aufzeigt. Darüber hinaus werden alternative Ansätze zur Lösung der verbleibenden Herausforderungen vorgeschlagen.



# Contents

<b>Abstract</b>	<b>i</b>
<b>Zusammenfassung</b>	<b>iii</b>
<b>Acronyms</b>	<b>xi</b>
<b>1. Introduction</b>	<b>1</b>
1.1. The Standard Model of Particle Physics . . . . .	1
1.2. The Future Circular Collider . . . . .	2
1.3. Possible Detector Concepts . . . . .	3
1.4. Detector Signatures . . . . .	4
1.4.1. Signatures of the $\tau$ Lepton . . . . .	5
<b>2. Machine Learning for <math>\tau</math> Lepton Jet Identification</b>	<b>7</b>
2.1. Introduction . . . . .	7
2.2. Data Generation . . . . .	7
2.2.1. Jet Clustering . . . . .	8
2.3. Particle Properties . . . . .	9
2.4. Simple Feed-Forward Neural Network . . . . .	10
2.5. Transformer Network . . . . .	11
<b>3. Evaluation of Machine Learning Models</b>	<b>13</b>
3.1. Independent Performance Evaluation . . . . .	13
3.1.1. Simple Feed-Forward Neural Network . . . . .	13
3.1.2. Particle Transformer Network . . . . .	16
3.2. Comparison of Models . . . . .	18
<b>4. Explicit Reconstruction of <math>\tau</math> Leptons</b>	<b>19</b>
4.1. Introduction . . . . .	19
4.1.1. Photon Masking . . . . .	20
4.2. Intermediate State Reconstruction . . . . .	20
4.2.1. $\pi^0$ Meson Reconstruction . . . . .	20
4.2.2. $\rho(770)^\pm$ Meson Reconstruction . . . . .	21
4.3. Decay Mode Reconstruction . . . . .	21
4.4. Generator Level Evaluation . . . . .	22
<b>5. Evaluation of Reconstruction Algorithms</b>	<b>25</b>
5.1. Jet Flavor Tagging Performance . . . . .	25

5.2.	Decay Mode Reconstruction Performance . . . . .	26
5.2.1.	Efficiency of the Cuts . . . . .	31
5.3.	Exclusion of FSR . . . . .	32
5.3.1.	Evaluation of the $\pi^0$ Reconstruction . . . . .	33
5.3.2.	Evaluation of the $\rho(770)^\pm$ Reconstruction . . . . .	33
5.4.	Summary . . . . .	34
<b>6.</b>	<b>Conclusion</b>	<b>35</b>
6.1.	Summary . . . . .	35
6.2.	Potential Future Work . . . . .	35
	<b>Bibliography</b>	<b>37</b>
<b>A.</b>	<b>Distributions of the Variables Used in the Analysis</b>	<b>41</b>
<b>B.</b>	<b>Performance Evaluation of ML-Models for Classifying <math>Z \rightarrow qq</math> Jets</b>	<b>45</b>
B.1.	ROC Curves for $Z \rightarrow qq$ Jets . . . . .	45
B.2.	Purity and Efficiency for $Z \rightarrow qq$ Jets . . . . .	49
<b>C.</b>	<b>Detailed Analysis of the Explicit Reconstruction Performance</b>	<b>53</b>
C.1.	Raw Jet Tagging Performance . . . . .	53
C.2.	Jet Energy Distributions . . . . .	53
C.3.	Distribution of the Reconstructed $\pi^0$ Candidate Mass . . . . .	54

# List of Figures

1.1.	Particles in the Standard Model . . . . .	1
1.2.	Future Circular Collider . . . . .	2
1.3.	CLD and ALLEGRO detectors . . . . .	3
1.4.	IDEA detector . . . . .	4
2.1.	Simple feed-forward neural network . . . . .	10
2.2.	Particle Transformer Network . . . . .	12
3.1.	Performance of the SimpleNN algorithm . . . . .	14
3.2.	Prediction distribution for output class $\tau$ across decay modes . . . . .	15
3.3.	Purity-efficiency of SimpleNN in $\tau$ jet identification with $Z \rightarrow qq$ background	16
3.4.	Performance of Particle Transformer Network for $\tau$ lepton identification with $Z \rightarrow qq$ background . . . . .	16
3.5.	Purity-efficiency of Particle Transformer Network in $\tau$ jet identification with $Z \rightarrow qq$ background . . . . .	17
3.6.	Performance of Particle Transformer Network for $\tau$ jet identification with $H/Z \rightarrow \tau$ Jets as Signal and $c$ -/ $b$ -Jet Background . . . . .	18
4.1.	Overview of $\tau$ lepton decay modes in explicit reconstruction framework .	19
4.2.	$\pi^0$ meson reconstruction . . . . .	21
5.1.	Jet flavor tagging performance using explicit reconstruction . . . . .	25
5.2.	Rates of reconstructed $\tau$ decay modes vs. branching ratios . . . . .	26
5.3.	Confusion matrices for explicit reconstruction (no cuts applied) . . . . .	27
5.4.	Confusion matrices for explicit reconstruction with angle cuts on jet properties	28
5.5.	Angle distributions between the generated $\tau$ lepton and the closest recon- structed jet . . . . .	28
5.6.	Confusion matrices for explicit reconstruction with angle cuts, jet energy, and charge cuts . . . . .	29
5.7.	Confusion matrices for explicit reconstruction with angle cuts, jet energy, charge, and neutral hadron cuts . . . . .	30
5.8.	Confusion matrices for explicit reconstruction with angle cuts, jet energy, charge, number of photons, and neutral hadron cuts . . . . .	31
5.9.	Efficiency of jet cuts in explicit reconstruction algorithms for different decay classes . . . . .	32
5.10.	Photon energy distribution in single and multi-photon jets . . . . .	33
5.11.	$\pi^0$ mass distribution for jets with and without FSR cut . . . . .	34

A.1. Distributions of the variables used in the analysis. (1/3) . . . . .	42
A.2. Distributions of the variables used in the analysis. (2/3) . . . . .	43
A.3. Distributions of the variables used in the analysis. (3/3) . . . . .	44
B.1. ROC curve of SimpleNN for $Z \rightarrow qq$ jet classification. Input features: KIN+PID	45
B.2. ROC curve of SimpleNN for $Z \rightarrow qq$ jet classification. Input features: KIN .	46
B.3. ROC curve of Particle Transformer for $Z \rightarrow qq$ jet classification. Input features: KIN+PID . . . . .	47
B.4. ROC curve of Particle Transformer for $Z \rightarrow qq$ jet classification. Input features: KIN . . . . .	48
B.5. Purity and efficiency of SimpleNN for $Z \rightarrow qq$ jet classification. Input features: KIN+PID . . . . .	49
B.6. Purity and efficiency of SimpleNN for $Z \rightarrow qq$ jet classification. Input features: KIN . . . . .	50
B.7. Purity and efficiency of Particle Transformer for $Z \rightarrow qq$ jet classification. Input features: KIN+PID . . . . .	51
B.8. Purity and efficiency of Particle Transformer for $Z \rightarrow qq$ jet classification. Input features: KIN . . . . .	52
C.1. Raw jet flavor tagging performance . . . . .	53
C.2. Jet energy distributions of $Z \rightarrow \tau\tau$ decay, with and without jet angle cut .	54
C.3. Jet energy distributions of $Z \rightarrow \tau\tau$ decay, with and without jet energy cut	54
C.4. Jet energy distributions of $Z \rightarrow \tau\tau$ decay, with and without jet charge cut .	55
C.5. Distribution of the reconstructed $\pi^0$ candidate mass . . . . .	55



# List of Tables

1.1.	Branching ratios of $\tau$ decay . . . . .	5
2.1.	MC events per decay mode . . . . .	8
2.2.	Overview of particle flow candidate variables . . . . .	9
5.1.	Number of generator labels . . . . .	27



# Acronyms

**R5** generalized  $k_T$  algorithm with  $R = 0.5$

**$k_{T2}$**   $k_T$  algorithm in the configuration with a total of 2 jets

**KIN+PID** input set with kinematic and PID properties

**KIN** input set with kinematic particle properties

**ALLEGRO** A Lepton coLLider Experiment with Granular calorimetry Read-Out

**BSM** physics beyond the Standard Model

**CERN** European organization for nuclear research, *Conseil Européen pour la Recherche Nucléaire*

**CLD** CLIC-like Detector

**CLIC** Compact Linear Collider

**ECAL** electromagnetic calorimeter

**FCC** Future Circular Collider

**FCC-ee** Future Circular Collider electron-positron

**FCC-hh** Future Circular Collider hadron-hadron

**FSR** final state radiation

**HCAL** hadronic calorimeter

**IDEA** Innovative Detector for Electron-positron Accelerator

**LEP** Large Electron-positron Collider

**LHC** Large Hadron Collider

**MC** monte carlo

**ML** machine learning

**MLP** multi layer perceptron

**PID** particle identification

**QCD** quantum chromodynamics

**QFT** quantum field theory

**RICH** ring imaging Cherenkov detector

**ROC** receiver operating characteristic

**SM** Standard Model of particle physics

# 1. Introduction

## 1.1. The Standard Model of Particle Physics

The Standard Model of particle physics (SM) is currently the most complete and accurate model to describe the fundamental particles and their interactions. As a model, it allows us to predict the outcome of various experiments with high precision [1]. The SM is a quantum field theory (QFT) that describes the electromagnetic, weak, and strong forces and is defined by a set of at least 26 free parameters [2]. However, there are still some open questions that the SM cannot answer and that motivate the search for physics beyond the Standard Model (BSM) [1]. Probing for new physics mandates the increase of precision in the measurements of the SM parameters and the search for deviations from the SM predictions.

The particles in the SM are categorized based on their properties and interactions, with fermions and bosons as the two main groups. Elementary fermions are further divided into quarks and leptons. The quarks are the building blocks of the hadrons and interact via the strong force, while leptons are neutral and charged particles that do not interact via the strong force. Leptons exist in three generations: the electron ( $e$ ) and electron neutrino ( $\nu_e$ ),

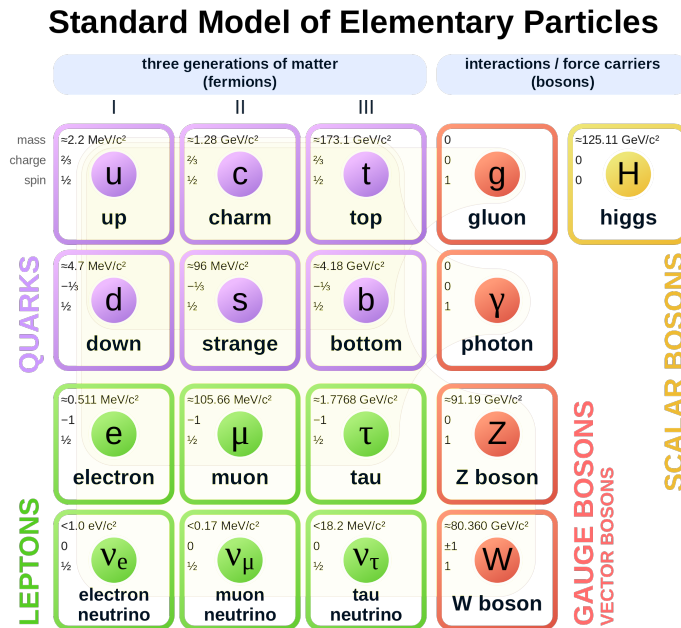


**Figure 1.1.:** The particles of the SM grouped by their type.

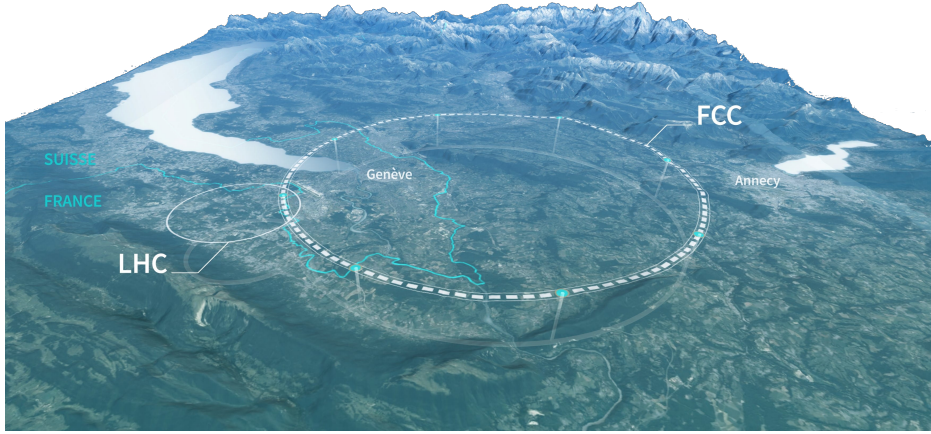


**Figure 1.2.:** The proposed layout of the Future Circular Collider (FCC) with a circumference of 90.7 km and an average depth of 200 m [6] (modified).

the muon ( $\mu$ ) and muon neutrino ( $\nu_\mu$ ), and the tau ( $\tau$ ) and tau neutrino ( $\nu_\tau$ ). Each generation consists of a charged lepton and a corresponding neutrino. The generations differ in mass, with particles in higher generations being heavier, but they all share the same charge and interaction properties. Bosons mediate the interactions of the SM and are responsible for the interactions between the particles. The elementary particles of the SM are shown in Figure 1.1.

The  $\tau$  lepton is the heaviest of the three charged leptons, with a mass of  $1777 \text{ MeV}/c^2$  and a lifetime of  $290 \times 10^{-15} \text{ s}$  [3]. Studying it is for example interesting because the  $\tau$  lepton is a common decay product for heavy electroweak particles and the identification is thus crucial to study various physics topics. Because of the universality of the electroweak interactions, the  $\tau$  lepton can also be used to study the properties of the other leptons. The  $\tau$  lepton is also a key ingredient in the search for BSM as its properties can be used to test the SM predictions [4]. One such example of finding BSM can be attained by analyzing the  $CP$  property of the Higgs boson. The decay of  $H \rightarrow \tau^+ \tau^-$  gives access to the  $CP$  properties of the boson by the measurement of the decay planes of the decaying  $\tau$  leptons. The relative angle between the decay planes is sensitive to the mixing angle between the  $CP$  even (predicted by the SM) and  $CP$  odd properties of the Higgs boson. As some decay modes of the  $\tau$  lepton are better suited for such analyses, finding the decay mode of the  $\tau$  lepton brings additional benefits[5].

## 1.2. The Future Circular Collider

To make further advances in the field of particle physics, a new collider at the European organization for nuclear research, *Conseil Européen pour la Recherche Nucléaire* (CERN) is proposed with a circumference of 90.7 km and an average depth of 200 m. Its location will be in the Geneva basin with surface points in France and Switzerland. The proposed layout of the FCC is shown in Figure 1.2. The FCC will run in multiple stages, with the first stage

being the Future Circular Collider electron-positron (FCC-ee) for precision measurements starting in the mid-2040s. It will be followed by the Future Circular Collider hadron-hadron (FCC-hh), reaching very high energies of  $\sqrt{s} \approx 100$  TeV [6]. This thesis will focus on the FCC-ee operated around the  $Z$  boson resonance with a center-of-mass energy of  $\sqrt{s} = 91.2$  GeV [4, 3]. During operation at the  $Z$  pole, an expected number of  $6 \times 10^{12}$   $Z$  bosons will be produced during the span of 4 years with an integrated luminosity of  $\mathcal{L} \approx 210 \text{ ab}^{-1}$  [7]. By using extensive data sets, the FCC-ee will be able to measure the properties of the  $Z$  boson and its decay products with unprecedented accuracy. For the parameters of the  $\tau$  lepton we can expect improvements in orders of magnitude compared to the current measurements [7].

### 1.3. Possible Detector Concepts

For making advances in the field of particle physics it is necessary to have a detector that can measure the properties of particles with high precision. Currently, there are three detector concepts proposed for the FCC [7].

1. CLIC-like Detector (CLD) [8]
2. Innovative Detector for Electron-positron Accelerator (IDEA) [8]
3. A Lepton coLLider Experiment with Granular calorimetry Read-Out (ALLEGRO) [9]

The CLD is based on the Compact Linear Collider (CLIC)-detector, which uses silicon pixel vertex detectors, silicon trackers and is followed by silicon-tungsten electromagnetic calorimeters (ECALs) and hadronic calorimeters (HCALs). The CLD detector concept is shown in Figure 1.3a. A precision of  $3 \times 3 \mu\text{m}^2$  in the vertex detection and a momentum resolution for high energy muons of  $\Delta(1/p_T) < 5 \times 10^{-5} \text{ c/GeV}$  could be reached [8].

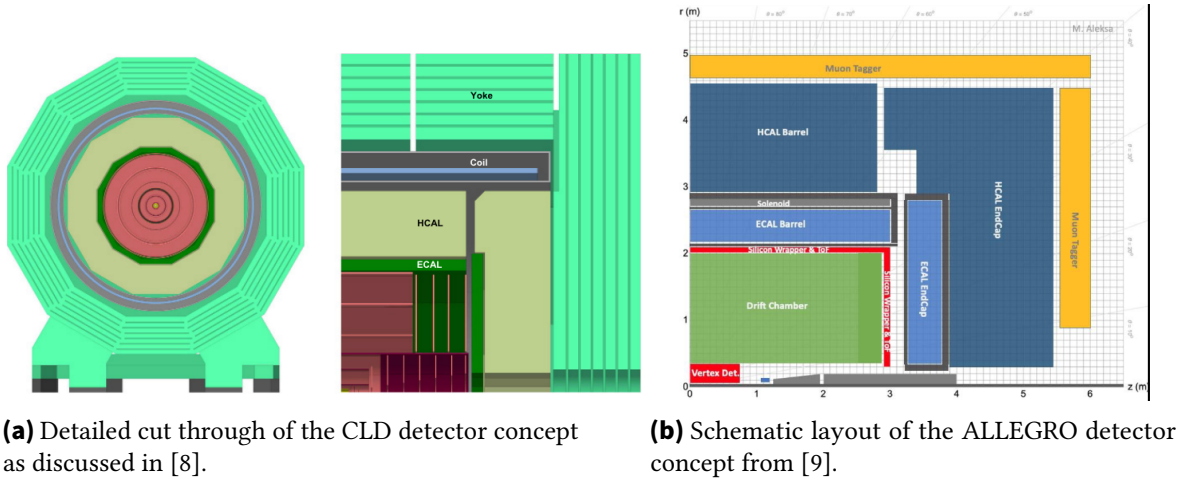
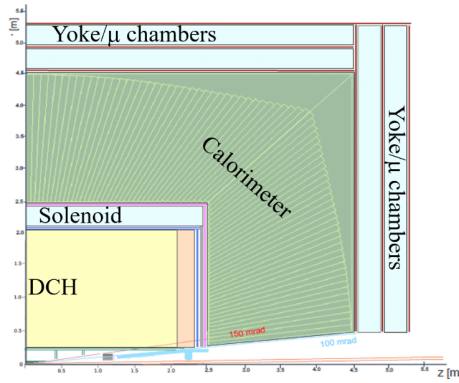
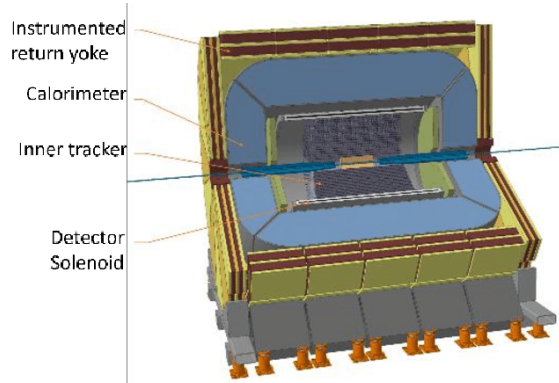


**Figure 1.3.:** Proposed structures of the CLD and ALLEGRO detectors.



(a) Schematic layout of the IDEA detector concept from [10].



(b) 3D model of the IDEA detector concept from [11].

**Figure 1.4.:** Proposed structure of the IDEA detector concept.

A second detector concept is the IDEA detector shown in Figure 1.4. It is also based on a silicon vertex detector at its core but is followed by a large volume wire drift chamber for particle identification and momentum measurement, based on ionization cluster counting. The drift chamber is surrounded by strip detectors, the solenoid a dual readout calorimeter, and muon chambers. Its vertex detector is assumed to have a resolution of  $5\text{ }\mu\text{m}$  [8]. This thesis focuses on the IDEA detector concept.

The newest detector concept is the ALLEGRO detector. Based on a noble liquid calorimeter it is designed to have a high granularity and thus good performance in particle identification. The detector concept is shown in Figure 1.3b. The rest of the setup is the same as the IDEA detector but with calorimeters based on liquid argon or krypton and measurement by ionization of the noble liquid atoms [9].

## 1.4. Detector Signatures

Detectors in collider experiments are used to measure the properties of the particles being produced. The properties which are collected can be divided into kinematic properties and information on particle identification. While some detector components may only focus on one of these areas, other components may collect information in both domains. On all of the detector concepts presented in the previous section, the first component a particle has to pass is a tracking detector. Tracking detectors are used to measure the spatial and temporal coordinates of the charged particles passing through them. In combination with a uniform magnetic field within the tracker volume, the curvature of the measured tracks may be used to determine the momentum of the particle as well as the charge [12].

To determine the total four vectors of the produced particle one secondly needs a measurement of the particle energy. The particle energy is measured using calorimeters. Calorimeters are composed of dense material forcing the passing particles to interact with the calorimeter. By measuring the energy released during interactions and summing it up the



total particle energy can be calculated if the total particle energy was deposited in the detector component. In all presented detector concepts there are two types of calorimeter: ECALs for particles mainly interacting via the electromagnetic interaction followed by the HCALs whose interaction length is much greater to also fully capture hadrons. As one might follow from the two names the calorimeters are therefore already indirectly useful to gather particle identifying information, as the main interaction type is encoded in the deposited energies in both calorimeter types. Secondly, the combination of measured momentum and energy may be used to calculate the particle energy and find further information on the exact type of particle [12].

As the particle type is a very crucial information for all physics analysis, further efforts are taken to gather more particle identification properties. Detecting muons may be one of the easiest tasks, as their interaction with matter is only minimal they are the only particles that can be detected outside the HCAL where muon traps are placed. Further ways to determine the particle type may be time-of-flight detectors like the one employed in ALLEGRO or the ionization information from the drift chamber planned in IDEA. Furthermore, ring imaging Cherenkov detectors (RICHs) may be used to determine the particle type and energy by the emitted Cherenkov radiation [12].

#### 1.4.1. Signatures of the $\tau$ Lepton

This thesis is focused on the identification of  $\tau$  leptons from the decay products that are observable in a future collider like the FCC-ee. The  $\tau$  leptons decay modes have been studied in past experiments like the Large Electron-positron Collider (LEP)[13], the BaBar experiment[14] and Belle[14, 15] and can be used to identify the  $\tau$  lepton in a detector. Given the high mass of  $\tau$ , it is the only lepton capable of hadronization. Due to the strong electromagnetic interaction of electrons and the very weak interaction of muons, these two types of charged leptons are easy to detect. The  $\tau$  lepton, on the other hand, is more difficult to detect. Its short lifetime requires more in-depth analysis to reconstruct the existence of  $\tau$  leptons from their decay products since they would have already decayed by the time they could interact with detector components.

**Table 1.1.:** Dominant branching ratios of the  $\tau$  lepton decay modes [3].  $h^\pm$  denotes either  $\pi^\pm$  or  $K^\pm$ .

Decay Mode	Branching Ratio
$\tau^- \rightarrow \mu^- \bar{\nu}_\mu \nu_\tau$	$(17.39 \pm 0.04) \%$
$\tau^- \rightarrow e^- \bar{\nu}_e \nu_\tau$	$(17.82 \pm 0.04) \%$
$\tau^- \rightarrow h^- \nu_\tau$	$(11.51 \pm 0.05) \%$
$\tau^- \rightarrow h^- \geq 1\pi^0 \nu_\tau$	$(36.51 \pm 0.09) \%$
$\tau^- \rightarrow h^- h^+ h^- \nu_\tau$	$(9.80 \pm 0.05) \%$
$\tau^- \rightarrow h^- h^+ h^- \geq 1\pi^0 \nu_\tau$	$(5.09 \pm 0.05) \%$
<b>Total</b>	$(98.12 \pm 0.14) \%$

The most prominent decay modes of the  $\tau$  lepton are listed in Table 1.1. Knowledge of the decay modes can be used to identify the  $\tau$  lepton in a detector and to measure its properties. To achieve this goal it is necessary to separate the decays of the  $\tau$  lepton from other processes. Background processes are those that occur in the collider experiment and can lead to similar collections of detectable particles. Possible background processes are the decays of heavy hadrons containing charm or bottom quarks.

Although the identification of this lepton flavor is challenging, especially against other fast decaying particles like quarks, the advantage of the FCC-ee is that it allows better results in these reconstructions than hadron colliders like the Large Hadron Collider (LHC)[4]. The main factor for the better reconstruction quality is the reduction of background events, resulting in a cleaner environment, in electron colliders. Furthermore, Hadron collisions are naturally convoluted due to quantum chromodynamics (QCD). The large number of showers produced by QCD challenges jet clustering and reconstruction algorithms, as it increases the total number of final state particles significantly[16, 4]. These algorithms are further challenged by a phenomenon known as pile-up. During a bunch collision at the LHC, dozens of protons pass each other and collide simultaneously, producing overlapping jets that must be separated for detailed analysis. All these factors are minimized in an electron-positron collider like the FCC-ee, allowing the use of simpler approaches for reconstruction algorithms.

## 2. Machine Learning for $\tau$ Lepton Jet Identification

### 2.1. Introduction

With advances in computing power and the development of new algorithms, machine learning (ML) became the state of the art in the last years. Jet flavor tagging poses large analytical challenges due to the nature of the processes at hand. Especially the very high number of final state profiles per jet flavor can make it hard to distinguish between different jet flavors.

Particularly in the case of proton-proton-collision experiments, like the LHC experiments at CERN, the high number of produced particles made it necessary to develop algorithms able to handle the most complex of these tasks [17].

Transitioning from the LHC to the FCC-ee the parameters for determining the optimal jet flavor tagging strategy change. The FCC-ee will produce a large number of  $Z$  bosons during the runs at the  $Z$  resonance, which will decay particularly cleanly into the final decay products, as discussed in subsection 1.4.1. The cleaner background may allow simpler algorithms to achieve the same level of performance as the more complex algorithms used at the LHC. The clear advantage of simpler algorithms being the reduced computational cost considering the large number of events produced at the FCC-ee (see section 1.2).

Based on this premise the goal of the following part of the thesis is to evaluate and compare the performance of two different ML algorithms for the task of  $\tau$  lepton identification. The algorithms will be evaluated based on their performance in identifying  $\tau$  leptons in a simulated detector environment. The performance of the algorithms will be evaluated in terms of their ability to identify  $\tau$  leptons and differentiate them from background processes. As an added benefit, the performance in distinguishing between the background processes themselves, can be evaluated.

### 2.2. Data Generation

The data used for the evaluation of the ML algorithms is generated using monte carlo (MC) simulation, with decays generated by Pythia8 [18]. Afterward, the detector response based on the IDEA detector is simulated using DELPHES [19]. The simulated events are saved in the

**Table 2.1.:** Number of MC events used of the generated MC decays for the different decay modes.

Use Case	Decay	Events for Training	Events for Testing
SimpleNN	$Z \rightarrow xx$	300 000	200 000
Particle Transformer	$Z \rightarrow \tau\tau$	400 000	100 000
Particle Transformer	$Z \rightarrow cc/bb$	800 000	200 000
Particle Transformer	$Z \rightarrow ss$	492 297	100 000
Particle Transformer	$Z \rightarrow uu/dd$	400 000	100 000
Particle Transformer	$H \rightarrow \tau\tau$	400 000	100 000
Particle Transformer	$H \rightarrow cc/bb$	400 000	100 000

EDM4hep format [20] and converted to flat ntuples using the FCCAnalyses Framework [21]. Most of the events are generated at the  $Z$  boson resonance with a center-of-mass energy of  $\sqrt{s} = 91$  GeV. The following decays of the  $Z$  boson are considered:

- $Z \rightarrow \tau^+\tau^-$
- $Z \rightarrow q\bar{q}$  with  $q \in \{u/d, s, c, b\}$

In the following,  $q$  will always denote an unspecified quark from the set  $\{u, d, s, c, b\}$ . Sometimes in the following text  $Z \rightarrow qq$  is used to denote  $Z \rightarrow q\bar{q}$  and  $Z \rightarrow \tau\tau$  is used instead of the more precise  $Z \rightarrow \tau^+\tau^-$ , with  $\tau$  in general denoting a  $\tau$  lepton of unspecified charge. For some analyses, the decay of the Higgs boson is studied as well. For the generation of the Higgs boson decays, the  $Z/H$  production at  $\sqrt{s} = 240$  GeV is used. The number of events used for the training on the different decay modes is shown in Table 2.1.

### 2.2.1. Jet Clustering

The detected particles are then clustered into jets using two different jet clustering algorithms. The  $k_T$  algorithm in the configuration with a total of 2 jets ( $k_T2$ ) [22, 23] (exclusive clustering) is used as well as the generalized  $k_T$  algorithm with  $R = 0.5$  ( $R5$ ) [22] (inclusive clustering). The  $k_T2$  algorithm is used to cluster the particles into exactly two jets, while the  $R5$  algorithm is used to cluster the jets according to the radius parameter  $R = 0.5$ . For both jet types the defining parameters of the jet, like the jet energy and momentum, are determined and the constituents of the jets are reconstructed using the Particle Flow Algorithm [24]. Histograms of the variables used in the analysis are shown in Appendix A. The key difference between the two algorithms is, that for the  $k_T2$  clustered jets, the number of jets is (mostly)<sup>1</sup> predetermined and fixed to two, while for the  $R5$  clustered jets the number of jets is not fixed and can vary between events. All jet clustering algorithms in the MC simulation were used like implemented in FastJet[22]. In the clustering, leptons with an energy greater than 15 GeV are masked.

---

<sup>1</sup>In certain edge cases  $k_T2$  is only able to produce a single jet.

**Table 2.2.:** Overview of particle flow candidate variables. All variable names are succeeded by the name of the jet algorithm used. Some variables were skipped due to insignificance in the analysis.

Symbol	Variable Name	Description
$E$	pfcand_e	Energy of the particle
$p$	pfcand_p	Momentum of the particle
$E_{rel}, \ln E_{rel}$	pfcand_ere1(_log)	Energy of particle relative to jet energy
$O_{ch}, O_y, \dots$	pfcand_is*	Particle type in one hot encoding (charged hadron, neutral hadron, muon, electron, gamma)
$Q$	pfcand_charge	Charge of the particle
$ID_{PDG}$	pfcand_type	PDG ID of the particle
$\Delta\theta, \Delta\phi$	pfcand_thetarel/_phirel	$\theta, \phi$ angle between jet and particle
$\theta, \phi$	pfcand_theta/_phi	$\theta, \phi$ angle of the particle
$\frac{dN}{dx}$	pfcand_dndx	Number of primary ionisation clusters
$m_{t.o.f.}$	pfcand_mtof	Mass of particle from time of flight
$d_z, d_{xy}$	pfcand_dz/_dxy	longitudinal/transverse impact parameter

For the ML algorithms, the jets clustered using the  $k_T2$  algorithm are used. This decision is based on the following premises: Due to the symmetric nature of the  $Z$  boson decay, we expect a back-to-back production of the daughter particles of the  $Z$  boson. The two jets produced using this clustering approach attempt to exploit the physical symmetries behind the decay by ideally separating the decay products into two hemispheres, thus allowing very early exploitation of known information about the decay. This will ensure that the jets produced will in most cases contain the products of a single decay of one of the daughter particles produced by the  $Z$  boson, allowing classification at the jet level rather than at the event level. A further argument can be made by using the results of the explicit reconstruction presented in section 5.1, where the  $k_T2$  algorithm performs significantly better than the  $R5$  on the raw input set<sup>2</sup>, as shown in section C.1. Lastly, the choice is underlined by a short evaluation of the performance of the Particle Transformer Network using the two different jet clustering algorithms, where the  $k_T2$  algorithm performs better than the  $R5$  algorithm.

## 2.3. Particle Properties

The variables calculated for each particle flow candidate are summarized in Table 2.2. Jet flavor tagging using ML algorithms is performed using a subset of these variables as

<sup>2</sup>Raw: No exclusion of jets based on their properties, similar to the ML approach.

input features. Two sets of input features are used, to compare the influence of particle identification (PID) on the results achievable. The input set with kinematic particle properties (KIN), contains only the kinematic variables of the particle flow candidates, i.e. the energy, momentum, and angles of the particles. The second set, input set with kinematic and PID properties (KIN+PID), contains all variables from Table 2.2 except  $ID_{PDG}$  and  $Q$ .

## 2.4. Simple Feed-Forward Neural Network

Due to the clean environment of the FCC-ee the first algorithm used for the  $\tau$  lepton identification is a simple feed-forward neural network, called *SimpleNN*. The goal of the study is to determine if such a limited approach can leverage the clean environment to achieve similar performance as the more complex Particle Transformer as introduced in section 2.1. The architecture of the neural network is shown in Figure 2.1.

It is composed of six hidden layers with 8 to 256 neurons respectively in descending order. The number of neurons in the first layer is determined by the number of input features used and is 227 for the KIN+PID input features and 105 for the KIN input features. As input features

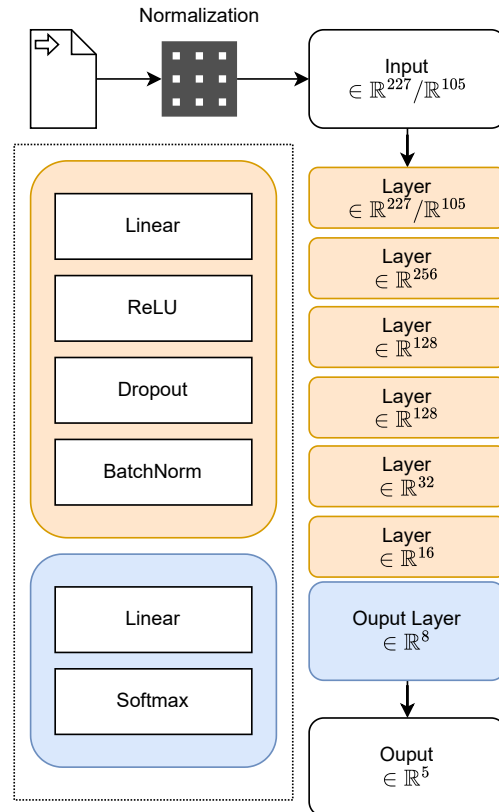


**Figure 2.1.:** Architecture of the simple feed-forward neural network used for the  $\tau$  lepton identification.

the variables from the particle flow candidates in the two different sets are used. Only the direction information of the particle candidates is removed from both sets. The rationale for the removal of directional data associated with particle candidates is based on the inherent inability of the underlying model to readily extract additional information, particularly with regard to the relative positions of individual particles. Furthermore, the rotational symmetry exhibited in the decays around the jet axis also impedes the acquisition of further information. The number of considered particle flow candidates is fixed to 15, padding the input with out-of-range values if there are less than 15 candidates, and truncating the input if there are more than 15 candidates. As the activation function the ReLU function is used. There are eight neurons in the output layer with the softmax activation function, resulting in five output classes. The hidden layers are followed by a dropout layer and a BatchNormalization layer. For the loss function, the Crossentropy loss function is used and the Adam optimizer is used for training. Implementation of the neural network is carried out using the PyTorch library [25].

## 2.5. Transformer Network

As a benchmark for the ML performance achievable with the current algorithms the Particle Transformer Network, by Qu, Li, and Qian implemented in [26] is used. The architecture of the network is shown in Figure 2.2. For testing and training of the network the framework *weaver-core* [27] is utilized. For a better match with respect to the architecture some of the input features are slightly altered, i.e. the relative transverse momentum is calculated from  $p$  and the relative angle, as well as the three momentum components instead of using  $p$ ,  $\theta$  and  $\phi$  directly.

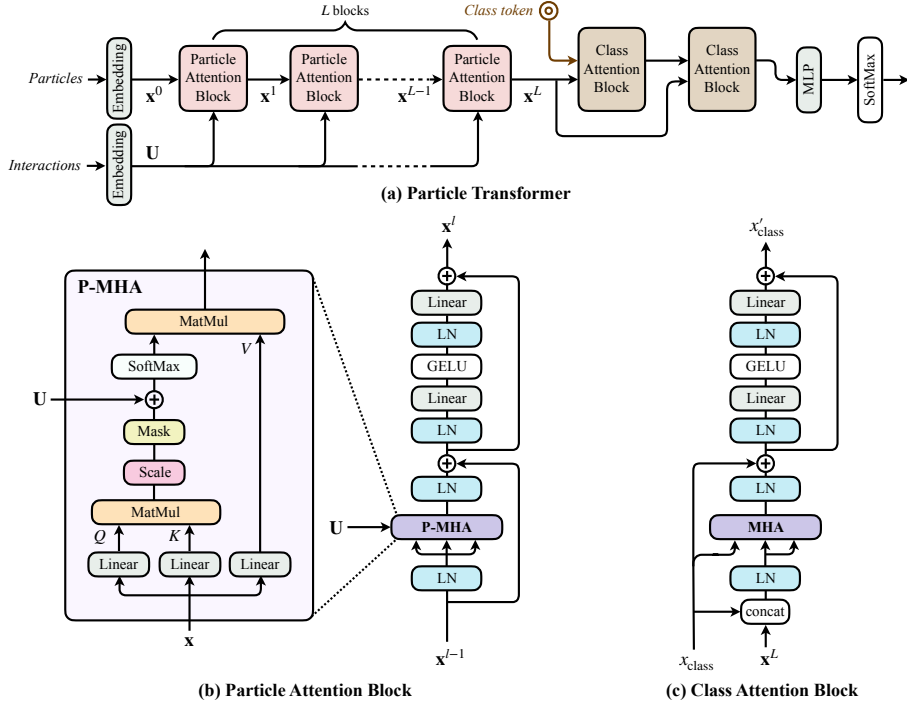


**Figure 2.2.:** Architecture of the Particle Transformer Network, as implemented in [26].

Particle Transformer is a transformer-based model that uses the particle interactions as inputs to the model. Particle Transformer can be viewed as a graph neural network with a fully-connected graph on all particles in a jet [26]. The  $N$  particles in the jet form a matrix  $X \in \mathbb{R}^{N \times D}$ , where  $D$  is the number of features for each particle. They are transformed using fully connected linear layers into matrix  $x_0$ . Out of these hidden features, key and query pairs are formed using a multi layer perceptron (MLP), each. The scalar product between key and query pairs defines an attention matrix  $A \in \mathbb{R}^{N \times N}$ . In addition an interaction input  $X' \in \mathbb{R}^{N \times N \times C}$  is calculated. It contains physics inspired particle relations such as angles and relative momenta. Finally  $X'$  is then transformed by an MLP into a matrix  $U \in \mathbb{R}^{N \times N}$  containing particle interaction features, added to  $A$  to form the final attention of one attention head.

The particle features  $x_0$  are then fed into a stack of  $L$  particle attention blocks with multi-head self-attention. The interaction matrix  $U$ , enriched with physics features, serves as a bias for the attention mechanism, making this a non-standard transformer. The attention score is calculated using the interaction features from  $U$ , which modulates the attention between particle features. The same set of interaction features is used across all particle attention blocks.

Finally, the results of these attention blocks are passed through a class attention block that uses multi-head attention to form the final output labels.



## 3. Evaluation of Machine Learning Models

The most important metrics for the evaluation of tagging algorithms in particle physics are the efficiency and the purity of the tagging. Efficiency is defined as

$$\mathcal{E} = \frac{TP}{TP + FN}, \quad (3.1)$$

where  $TP$  denotes the number of true positives and  $FN$  is the number of false negatives. While the purity is defined as

$$\mathcal{P} = \frac{TP}{TP + FP}, \quad (3.2)$$

where  $FP$  denotes the number of false positives [28]. Furthermore the receiver operating characteristic (ROC)-curve is used to evaluate the performance of the algorithms, showing the dependence between the  $TPR$  and the  $FPR$ . The true positive rate is defined as

$$TPR = \frac{TP}{TP + FN} = \mathcal{E} \quad (3.3)$$

and the false positive rate is defined as

$$FPR = \frac{FP}{FP + TN}. \quad (3.4)$$

In this definition,  $TN$  stands for the number of true negatives. The ROC-curve is then used to evaluate the performance of the algorithms [29]. The area under the ROC-curve is used as a metric to compare the performance of the algorithms. The area under the ROC-curve is given by

$$AUC = \int_0^1 \mathcal{E}(FPR) dFPR. \quad (3.5)$$

### 3.1. Independent Performance Evaluation

#### 3.1.1. Simple Feed-Forward Neural Network

The ROC-curve for the jet tagging of the jets originating from the  $Z \rightarrow \tau\tau$  decay is shown in Figure 3.1. The performance of the algorithm is evaluated on a one-by-one basis against each type of the  $q$ -jets. This means that for the creation of all the curves in the plot, a

### 3. Evaluation of Machine Learning Models

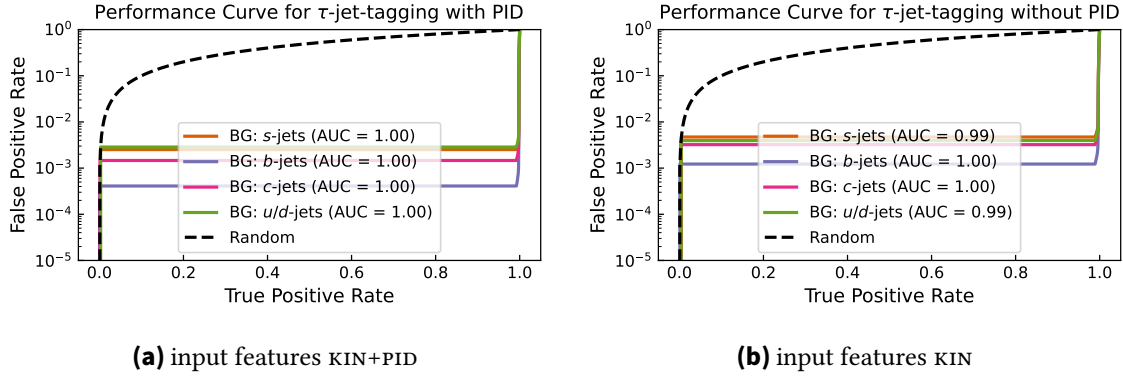


**Figure 3.1.:** Performance of the SimpleNN algorithm for the  $\tau$  lepton identification. The performance is evaluated on a one-by-one basis with background by the  $Z \rightarrow qq$  decays.

selection was applied on the studied jets to only consider those jets whose true flavor  $\mathcal{F}$  follows

$$\mathcal{F} \in \{\tau, x\}, \quad (3.6)$$

where  $x$  is the flavor, which is currently studied as the background.

The ROC-curves show a good performance with the  $FPR$  leveling out at a value of approximately  $10^{-3}$  for the KIN+PID input features and around to  $10^{-2}$  for the KIN input features. The horizontal line at those thresholds indicates an irreducible fake identification of the jets. To expand on the complete false identification it is worthwhile to look at the distribution of the prediction for the output class  $\tau$  for the jets stemming from the different decay modes. The distribution is shown in Figure 3.2. Taking the ratio between the end bins of the distribution for each of the jet flavors gives the misidentification rate. The clear rise in the bin with the highest prediction value for the  $q$ -jets indicates the confidence of the algorithm in the false identification of the jets.

In a previous iteration of the study, the predictive capacity of the model was assessed when the number of hidden layers in the network was reduced to three. In addition to the decline in tagging performance associated with a reduction in the number of tunable parameters in the model, a second observation was made, which ultimately led to the decision to utilize a larger neuron set. A reduction in the number of hidden layers to three resulted in a notable decline in model performance for the larger feature set, in comparison to the smaller input set. This suggests that with a smaller number of free parameters in the model, the model is unable to fully leverage the additional information present in the KIN+PID input features. This criterion plays a significant role in the decision to utilize a larger set of neurons and layers in the model.

The ROC-curves for evaluation of the performance of quark jet tagging using SimpleNN are listed in Appendix B. While the  $FPR$  for  $\tau$  jets being identified as  $q$  jets is very low at around  $10^{-3}$  to  $10^{-4}$  the misidentification between the quark flavors is very high. Especially when using the reduced set of particle features there is hardly any separation towards a random classifier. Using the full set of particle features the performance is better, reaching a  $FPR$  in the order of approximately  $10^{-1}$  for the quark flavor identification.

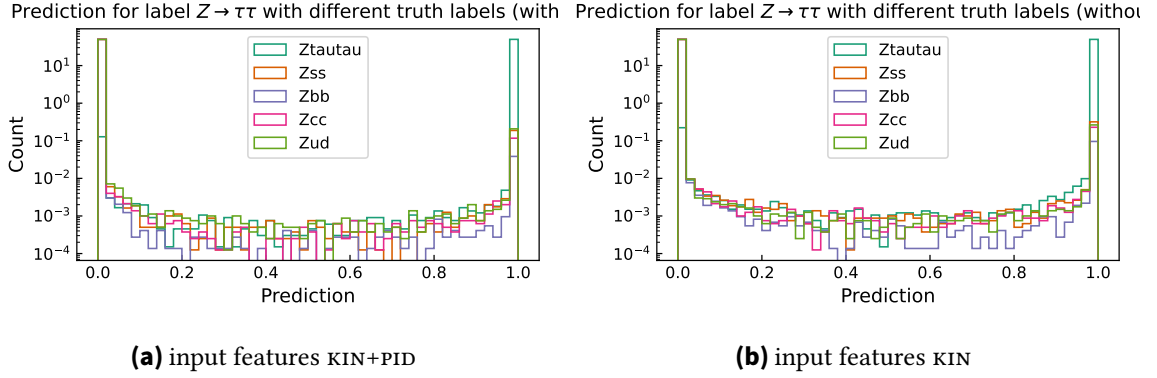


**Figure 3.2.:** Distribution of the prediction for the output class  $\tau$  for the jets stemming from the different decay modes.

Lastly, the performance of the jet tagging using the SimpleNN algorithm can be evaluated using the efficiency and purity defined above. For the context of purity and efficiency, normalization is important, as it defines the physics space in which our question is answered. The purity can be written as

$$\mathcal{P} = \frac{\mathcal{E}_\tau N_\tau \frac{\mathcal{L} \cdot \sigma_{Z \rightarrow \tau\tau}}{N_\tau}}{\mathcal{E}_\tau N_\tau \frac{\mathcal{L} \cdot \sigma_{Z \rightarrow \tau\tau}}{N_\tau} + \sum_{i \in \text{BG}} \mathcal{E}_i N_i \frac{\mathcal{L} \cdot \sigma_{Z \rightarrow ii}}{N_i}} \quad (3.7)$$

$$= \frac{\mathcal{E}_\tau \cdot Br(Z \rightarrow \tau\tau)}{\mathcal{E}_\tau \cdot Br(Z \rightarrow \tau\tau) + \sum_{i \in \text{BG}} \mathcal{E}_i \cdot Br(Z \rightarrow ii)},$$

with  $N_k$  being the number of jets in the class  $k$  and  $\mathcal{E}_k$  being the efficiency of the class  $k$ . Furthermore, we used that

$$\sigma_{Z \rightarrow kk} \propto \sigma_Z \cdot Br(Z \rightarrow kk), \quad (3.8)$$

where  $\sigma_Z$  is the cross-section of the  $Z$  boson production, being the same for all decay modes. In the context of jet tagging it thus follows to define the weights for the normalization, as the branching ratios of the  $Z$  boson decays. Using the numbers from [3] we get an estimate for the number of correct and incorrect identifications of jets in the actual run of the FCC-ee. The purity-efficiency curve for the SimpleNN algorithm is shown in Figure 3.3.

Again one can see the limit for the purity limited by the misidentification at a purity of 97 %. Notably, the efficiency is still very high at this point with a value of approximately 0.95 for the KIN input features and even higher for the KIN+PID input features. The purity-efficiency curve for the quark flavor identification is also shown in Appendix B in section B.2. SimpleNN is able to achieve an approximate purity of  $\mathcal{P} \approx 90\%$  for the quark flavor identification.

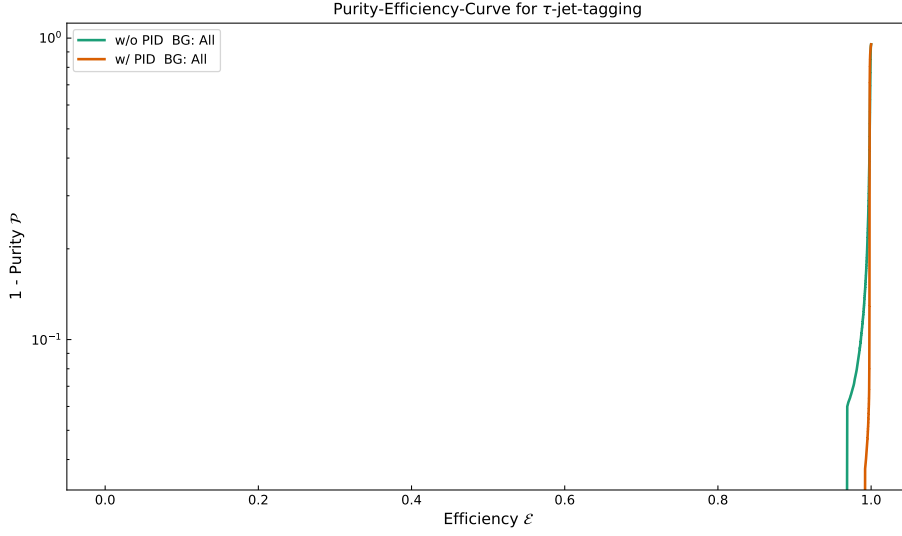


**Figure 3.3.:** Purity-efficiency curve for the SimpleNN algorithm for the  $\tau$  jet identification with background by the jets stemming from the  $Z \rightarrow qq$  decays.

#### 3.1.2. Particle Transformer Network

Evaluating the capacity of the Particle Transformer Network for the  $\tau$  lepton identification the ROC-curves are shown in Figure 3.4. The performance is evaluated on a one-by-one basis against each type of  $Z \rightarrow qq$  decays. The ROC-curves show a very good potential with the  $FPR$  being in the range of  $10^{-4}$  to  $10^{-5}$  for most of the  $TPR$  range for the  $KIN+PID$  input features and less than  $10^{-4}$  for the  $KIN$  input features.

Secondly, the performance for  $\tau$  jet identification hugely outperforms the results achieved for the quark flavor identification. The ROC-curves for evaluation of the performance of quark jet tagging using the Particle Transformer Network are also listed in Appendix B. Comparing the input sets  $KIN+PID$  and  $KIN$ , the quark separation is helped hugely by the

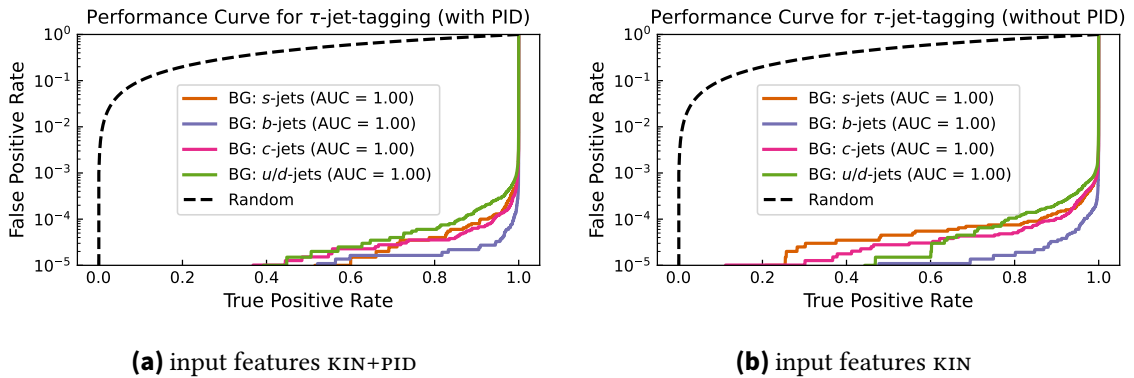


**Figure 3.4.:** Performance of the Particle Transformer Network for the  $\tau$  lepton identification. The performance is evaluated on a one-by-one basis with background by the  $Z \rightarrow qq$  decays.

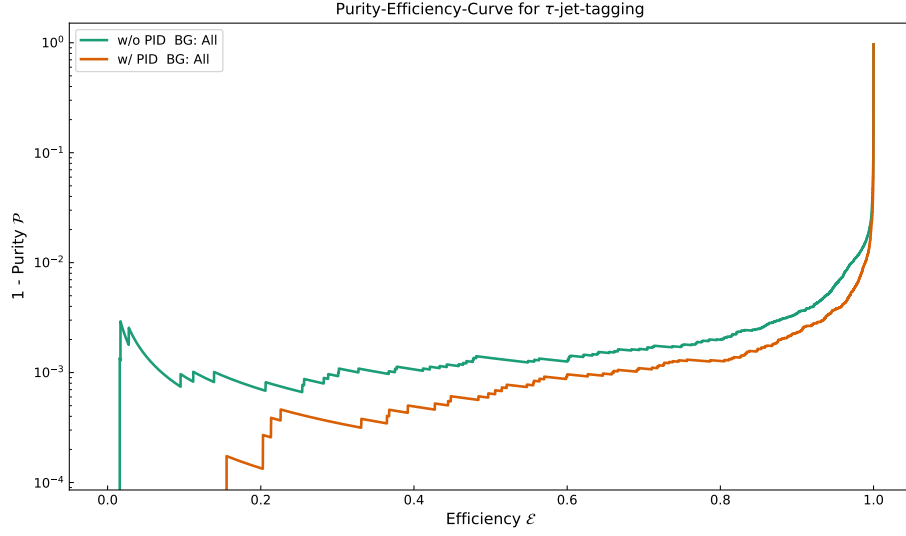


**Figure 3.5.:** Purity-efficiency curve for the Particle Transformer Network for the  $\tau$  jet identification with background by the jets stemming from the  $Z \rightarrow q\bar{q}$  decays.

particle identification information. The correctness for the  $\tau$  jet identification is not as much influenced by the particle identification information. Using the Particle Transformer Network allows for a  $FPR$  of approximately  $10^{-2}$  for the quark flavor identification.

The purity-efficiency curve for the Particle Transformer Network is shown in Figure 3.5. The performance of the Particle Transformer Network is evaluated using the same normalization as for the SimpleNN algorithm. The purity-efficiency curve shows a very high efficiency for the  $\tau$  jet identification with a purity of up to  $\mathcal{P} \approx 1 - 10^{-4}$ . The purity for the quark flavor identification in jet tagging is not as high, but still very good with a purity of  $\mathcal{P} \approx 99\%$  with particle identification information (see Figure B.7) and up to  $\mathcal{P} \approx 90\%$  without particle identification information (see Figure B.8).

#### 3.1.2.1. Particle Transformer Network for Higgs Boson Decays

Testing the jet identification potential of the trained Particle Transformer Network further, the performance of the network is evaluated on the identification of jets produced in MC samples of the decay of the Higgs boson. The training state of the model is used, without any further training on the Higgs boson decay samples. The ROC-curves for the identification of the jets stemming from the  $H \rightarrow \tau\tau$  decay are shown in Figure 3.6. The performance is evaluated on a one-by-one basis against jets from Charm and Bottom quarks. For comparability, the ROC-curves for the same quark flavors after the  $Z$  boson decay are also shown. Furthermore, this analysis is only focused on the  $\mathbf{KIN}$  input features.

The model performs with a very similar  $FPR$  for the identification of the  $H \rightarrow \tau$  jets as for the  $Z \rightarrow \tau$  jets. As expected the performance for the jets produced during  $Z$  decays

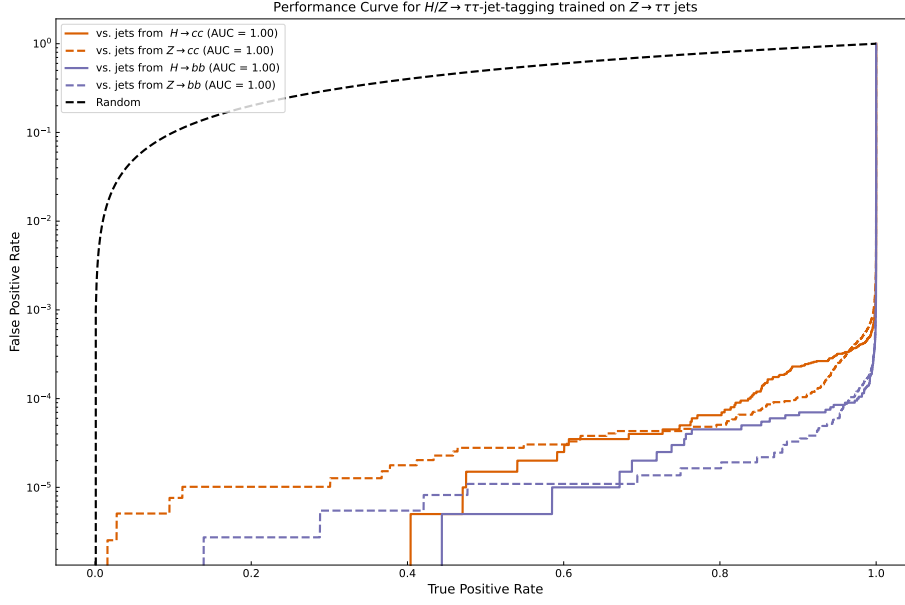


**Figure 3.6.:** Performance of the Particle Transformer Network for the  $\tau$  jet identification. The performance is evaluated on a one-by-one basis with  $H \rightarrow \tau$ - and  $Z \rightarrow \tau$ -jets as signal and background from  $c$ - and  $b$ -jets.

performs slightly better, as the model is tuned for analyzing these jets. Both the  $c$ - and  $b$ -jets are identified with a  $FPR$  of approximately  $10^{-4}$  up to  $10^{-5}$ .

## 3.2. Comparison of Models

Comparing the SimpleNN and Particle Transformer Models the large superiority with respect to false positives in  $\tau$  jet tagging is evident. The Particle Transformer Network is able to achieve a  $FPR$  of approximately  $10^{-5}$  for the  $\tau$  jet identification, while the SimpleNN algorithm is only able to achieve a  $FPR$  of approximately  $10^{-3}$ . The performance for the quark flavor identification is also better for the Particle Transformer Network, with a  $FPR$  of approximately  $10^{-4}$  compared to the  $FPR$  of approximately  $10^{-2}$  for the SimpleNN algorithm. This aspect is also reflected in the purity-efficiency curves for the two algorithms. The much higher purity for the Particle Transformer Network makes it the better choice for applications where the  $\tau$  jet identification with a high purity is needed.

On the other hand, the SimpleNN algorithm is able to achieve similar levels of efficiency in the tagging of  $\tau$  jets at a relatively low purity of 97 %, which can be useful in applications where high throughput is needed, but the purity is not as important. Although the throughput performance of both models was not evaluated due to the lack of a suitable framework, the SimpleNN algorithm is expected to have a higher throughput due to its simpler architecture. When comparing the performance in the realm of quark jet flavor identification the Particle Transformer Network has the clear upper hand on SimpleNN.

## 4. Explicit Reconstruction of $\tau$ Leptons

### 4.1. Introduction

To gain more insight into the decay of  $\tau$  leptons the approach of explicit reconstruction may also be used. Explicit reconstruction is the process of reconstructing the decay of a particle by using known decay modes and the properties of those decays. In the case of  $\tau$  leptons, the decay modes are well known and can be used to reconstruct the decay of the  $\tau$  lepton. The most important decay modes were already introduced in Table 1.1, a full overview of the decay modes implemented in the explicit reconstruction in this thesis is given in Figure 4.1.

Explicit reconstruction algorithms have the need for a very small number of wrongly identified particles, as the identified particles are used directly without further selections or probabilistic approaches. This condition will be met at the FCC-ee as explained in subsection 1.4.1.

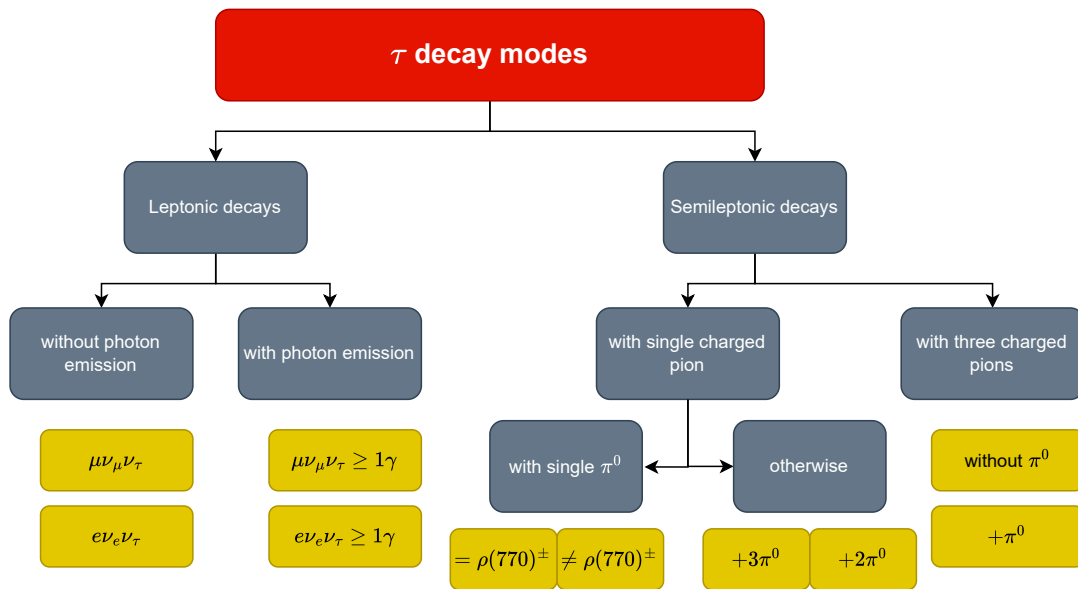


**Figure 4.1.:** Schematic overview of the decay modes of the  $\tau$  lepton implemented in the explicit reconstruction framework.

The explicit reconstruction is mainly based on counting the number of particles of a certain type in the decay products of the  $\tau$  lepton. This number of particles of a certain type is then used to determine the decay mode of the  $\tau$  lepton. One challenge in the case of the  $\tau$  lepton is the existence of intermediate particles like the  $\pi^0$  meson in the decay chain, which will decay before reaching the detector. Therefore, as a first step, the intermediate particles can be recovered to allow for a more accurate reconstruction.

For the explicit reconstruction, the dataset introduced in section 2.2 is used again, with the distinction, that the masking of highly energetic leptons is disabled. Thus nearly full comparability between the ML algorithms and the explicit reconstruction is given. The explicit reconstruction is carried out using a self-developed framework in Python.

### 4.1.1. Photon Masking

Charged particles may emit photons in the detector, for example, due to final state radiation (FSR). These photons can be reconstructed as separate particles in the detector. To account for this effect, the photons are masked in the explicit reconstruction. A cut is applied to ignore all photons with an energy below a threshold of 200 MeV. The evaluation of this cut value is explained in section 5.3. Masking those gamma particles logically leads to a drastic reduction in the precision of the decay modes which specifically include FSR photons, namely the decays  $\tau \rightarrow \ell \nu \nu \gamma$  with  $\ell \in \{e, \mu\}$ . To compensate for this, the masking is turned off for the reconstruction of these decay modes.

## 4.2. Intermediate State Reconstruction

### 4.2.1. $\pi^0$ Meson Reconstruction

The  $\pi^0$  meson exhibits a very short lifetime of approximately  $8.43 \times 10^{-17}$  s, after which it decays into two photons in 98.8 % of the cases [3]. The decay of the  $\pi^0$  meson can be reconstructed by searching for two photons with an invariant mass close to the mass of the  $\pi^0$  meson. Thus the reconstruction is carried out in two steps, as displayed in Figure 4.2.

First, all photons are identified and moved into a graph. The graph is then fully connected by the invariant mass of the pairs of photons. Afterward, the edges in the graph are iterated over in the order of the smallest deviation from the mass of the  $\pi^0$  meson. The photons which are connected by the edge with the smallest deviation are then removed from the graph and the edge is kept as a reconstructed  $\pi^0$  candidate. This process is repeated until no more edges are left in the graph or until the deviation of the edge is larger than a threshold extracted by a fit to the  $\pi^0$  mass peak. A maximum deviation of 103 MeV/c<sup>2</sup> is allowed. The fit using a Breit-Wigner function is shown in section C.3.



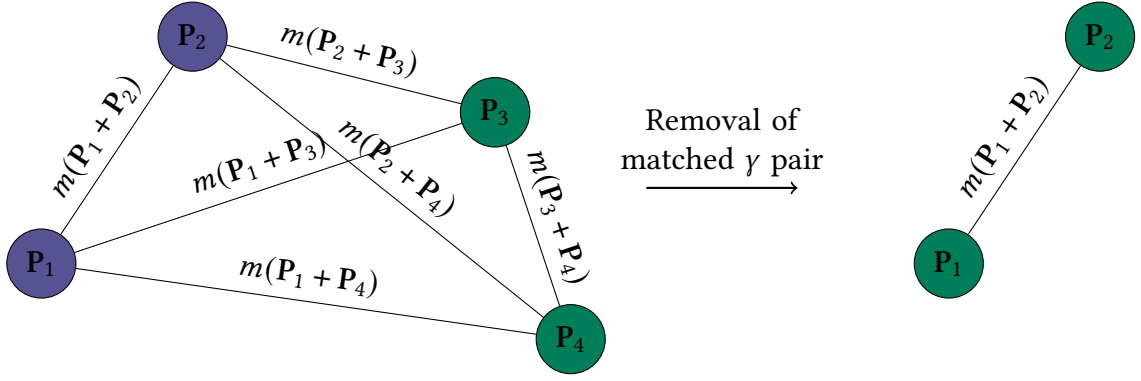


**Figure 4.2.:** Schematic graph for the  $\pi^0$  meson reconstruction. The nodes represent the photons with their 4-vector  $\mathbf{P}_i$  and the edges the invariant mass of the photon combinations. The pair of photons with the smallest deviation from the  $\pi^0$  mass in each step is marked in green.

#### 4.2.2. $\rho(770)^\pm$ Meson Reconstruction

The reconstruction above can be reused, for example, to reconstruct the  $\rho(770)^\pm$  meson. The  $\rho(770)^\pm$  meson decays into a  $\pi^\pm$  and a  $\pi^0$  meson in approximately 100 % of the cases [3]. To reconstruct the meson we thus search for combinations of charged hadrons and  $\pi^0$  mesons with an invariant mass close to the mass of the  $\rho(770)^\pm$  meson. The reconstruction is then carried out by identifying all possible combinations of charged hadrons and  $\pi^0$  mesons and calculating the invariant mass of the resulting pairs. Pairs with an invariant mass whose deviation to the mass of the  $\rho(770)^\pm$  meson is small enough are then preserved as reconstructed  $\rho(770)^\pm$  candidates. All candidate mesons within a tolerance band of  $252 \text{ MeV}/c^2$  around the mass of the  $\rho(770)^\pm$  meson are retained. For simplistic reasons, the mass tolerance band is the same as for the  $\pi^0$  meson reconstruction, with an addition of the mass width of the  $\rho(770)^\pm$  meson at  $149.1 \text{ MeV}/c^2$  [3].

### 4.3. Decay Mode Reconstruction

The main task of the reconstruction is based on a decision tree that checks the number of particle flow candidates of a certain type in the decay products of the  $\tau$  lepton. For this, multiple classes of decays are defined based on similarities between the decays. In this thesis the following classes for  $\tau$  decays are implemented:

- $\tau^- \rightarrow \ell^- \bar{\nu}_\ell \nu_\tau \geq 0\gamma$  with  $\ell \in \{e, \mu\}$
- $\tau^- \rightarrow 3\pi^\pm \nu_\tau \geq 0\pi^0$
- $\tau^- \rightarrow \pi^- \nu_\tau \geq 0\pi^0$

The categorization for a leptonic decay demands the presence of exactly one electron or muon in the decay products. Furthermore, no hadrons may be reconstructed in the evaluated jet. Subclassification is then performed based on the presence of a muon or

electron and whether at least one photon is present in the decay products that form the subclassifications

$$\tau^\pm \rightarrow \nu_\tau \begin{cases} e^\pm \bar{\nu}_e & \text{if } \exists e^\pm \begin{cases} 0\gamma & \text{if } \nexists \gamma \\ \geq 1\gamma & \text{otherwise} \end{cases} \\ \mu^\pm \bar{\nu}_\mu & \text{if } \exists \mu^\pm \end{cases} . \quad (4.1)$$

The photons present in the decay products may specifically be due to FSR or initial state radiation in accordance with the publication of the Belle Collaboration [15].

For the reconstruction of the decays involving pions the number of charged hadrons is counted and either the decay with exactly one charged pion is chosen or the decay with three charged pions is chosen. The subclassification is then carried out based on the number of  $\pi^0$  mesons in the decay products. For this, the intermediate reconstruction of the  $\pi^0$  mesons is used (see subsection 4.2.1). Especially for the case of three charged hadrons, the subclassification is again straightforward

$$\tau^\pm \rightarrow \pi^\pm \pi^\pm \pi^\mp \nu_\tau \begin{cases} 0\pi^0 & \text{if } \nexists \pi^0 \\ \geq 1\pi^0 & \text{otherwise} \end{cases} . \quad (4.2)$$

In the case of only a single charged hadron and the existence of a  $\pi^0$  meson the  $\rho(770)^\pm$  reconstruction is used to determine whether the decay  $\tau^\pm \rightarrow \pi^\pm \pi^0 \nu_\tau$  involved a  $\rho$  intermediate state. Deciding the subclassification is then based on the following schema

$$\tau^\pm \rightarrow \pi^\pm \nu_\tau \begin{cases} \pi^0(\rho(770)^\pm) & \text{if } \exists \rho(770)^\pm \\ \pi^0(\neq \rho(770)^\pm) & \text{if } \nexists \rho(770)^\pm \wedge 1\pi^0 \\ 2\pi^0 & \text{if } 2\pi^0 \\ 3\pi^0 & \text{if } 3\pi^0 \end{cases} . \quad (4.3)$$

## 4.4. Generator Level Evaluation

To evaluate the performance of the algorithms employed in this thesis, the truth information from the MC simulation is used. The truth information contains the information about the decay modes for both of the primary  $\tau$  leptons generated during the  $Z/H \rightarrow \tau\tau$  decay simulation. The following classes of decays are defined for the evaluation of the algorithms:

- $\tau^- \rightarrow \ell^- \bar{\nu}_\ell \nu_\tau$  for all  $\ell \in \{e, \mu\}$  as well as  $\tau^- \rightarrow \ell^- \bar{\nu}_\ell \nu_\tau \geq 1\gamma$  for all  $\ell \in \{e, \mu\}$
- $\tau^- \rightarrow \pi^- \nu_\tau$  as well as  $\tau^- \rightarrow \pi^- \nu_\tau \geq 1\gamma$
- $\tau^- \rightarrow \pi^- \pi^+ \pi^- \nu_\tau$  as well as  $\tau^- \rightarrow \pi^- \pi^+ \pi^- \nu_\tau \geq 1\gamma$

The photons produced in the decay can either be due to FSR or due to the decay of intermediate particles, such as the  $\pi^0$  meson. Since the generator information cannot be mapped directly to the reconstructed jets, the following mapping scheme is used: For all generated primary leptons, the angle between the momentum of the  $\tau$  and the momentum of all reconstructed jets is calculated. The jet with the smallest angle is then assigned to the generated  $\tau$  lepton. This smallest angle is now called  $\Delta\alpha$ . If a jet is linked to more than one  $\tau$  lepton, the jet is assigned to the  $\tau$  lepton with the smallest angle. If a jet is not paired with any  $\tau$  lepton, an empty generator tag is applied to the jet. The generator tag is then used to evaluate the performance of the reconstruction algorithms.



## 5. Evaluation of Reconstruction Algorithms

### 5.1. Jet Flavor Tagging Performance

While the implemented algorithms are not directly built for flavor tagging, their jet flavor tagging performance can still be evaluated by running the analysis on the jets originating from  $Z \rightarrow qq$  decays. In comparison to the ML algorithms, the explicit reconstruction algorithms in the implementation for the  $\tau$  lepton identification do not aim to discriminate between different quark flavors. Quark flavor tagging is an additional benefit provided by ML, but it is not a primary goal of  $\tau$  lepton identification. The relative numbers of jets being identified as decay modes of a  $\tau$  lepton are shown in Figure 5.1. Logically, a small number of tagged jets in the  $q$ -jets is wanted, while a high number of tagged jets in the  $\tau$  jets is desired.

To allow for a fair analysis of the results a cut was applied on the jets, based on the angle to the closest other jet in the event. This cut is motivated in the following section. All jets

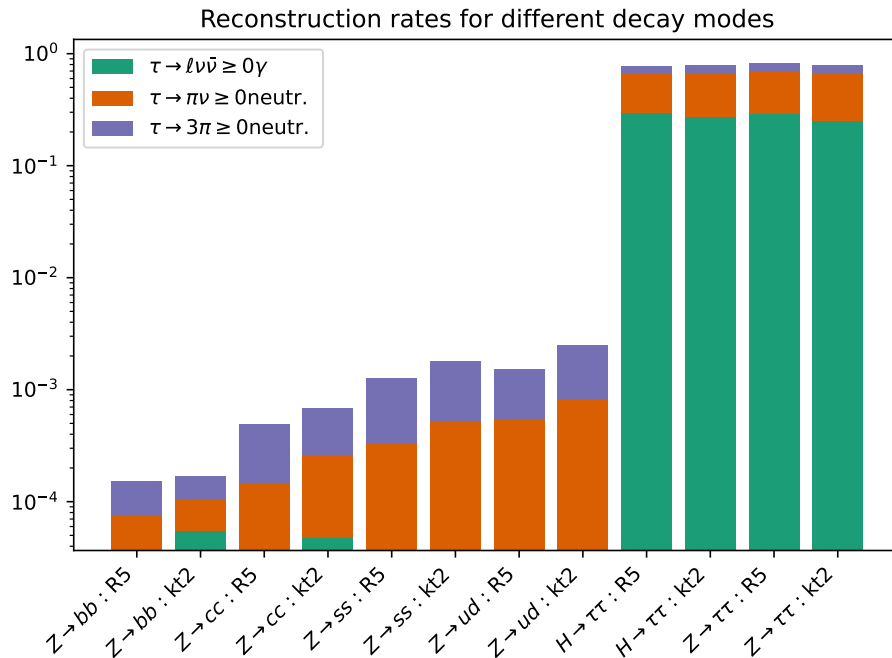


**Figure 5.1.:** Jet flavor tagging performance of the explicit reconstruction algorithms. The  $x$ -axis shows the true origin of the jets analyzed. The  $y$ -axis shows the relative rate of positive  $\tau$  reconstructions.

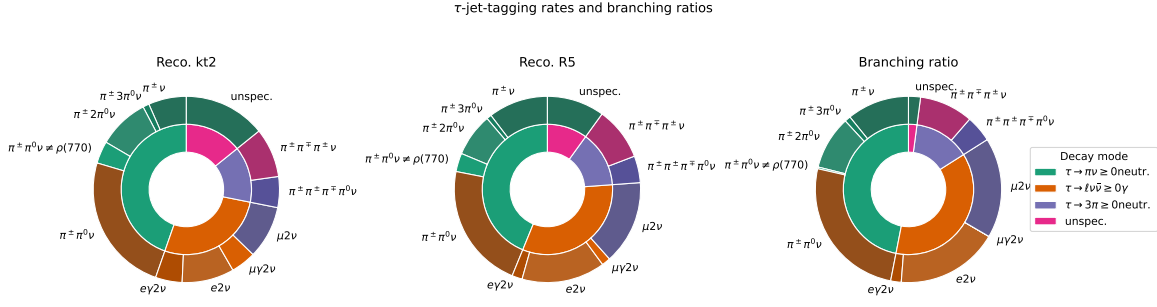


**Figure 5.2.:** Rates of reconstructed decay modes of the explicit reconstruction algorithms in comparison to the branching ratios of the  $\tau$  lepton.

whose closest neighbor is closer than a threshold angle  $\Delta\alpha_{\text{jet}}$  are rejected. For the events at the  $Z$  resonance the cut is set to  $\Delta\alpha_{\text{jet}} = 3.0$  rad, while for the events at the  $Z/H$  resonance the cut is set to  $\Delta\alpha_{\text{jet}} = 2.0$  rad. The reduction in the cut threshold for those events is due to the kinematics of the  $e^+e^-$  collisions where the Higgs boson is not produced at rest but with a discernible transverse momentum. The result for this analysis without the application of cuts is shown in section C.1.

Further cuts may be applied, reducing the background rates in the  $\tau$  jets further, but were omitted in this analysis due to time constraints. Using the cut on the angle to the closest neighbor the performance of the explicit reconstruction algorithms can be evaluated. While the efficiency for the  $\tau$  jet identification is quite high at up to 90 % (see subsection 5.2.1) the rejection of the background jets also leads to a high purity of the  $\tau$  jets. An approximate  $FPR$  of  $10^{-3}$  is achieved for the quark jet rejection. Especially the performance for the rejection of the heavy quark jets is very good, with a  $FPR$  of as low as  $10^{-4}$ .

## 5.2. Decay Mode Reconstruction Performance

A short overview of the performance of the algorithms to identify the decay modes of the  $\tau$  lepton can be achieved by comparing the rates of the reconstructed decay modes to the branching ratios of the  $\tau$  lepton. This comparison is shown in Figure 5.2.

For a more detailed analysis, it is important to not only observe the relative rates of jets being identified as a certain decay mode but also the correlation between the simulated decay mode and the reconstructed decay mode. For this analysis confusion matrices are used. Confusion matrices show the (normalized) number of jets, stemming from a certain decay mode at the generator level, being identified as a certain decay mode at the reconstruction level. Without applying any restrictions on the jets, the confusion matrices for the explicit reconstruction algorithms are shown in Figure 5.3. All confusion matrices are normalized on the  $y$ -axis, i.e. the number of jets stemming from a certain decay mode at the generator level. Jets rejected due to cuts are excluded in the normalization step.

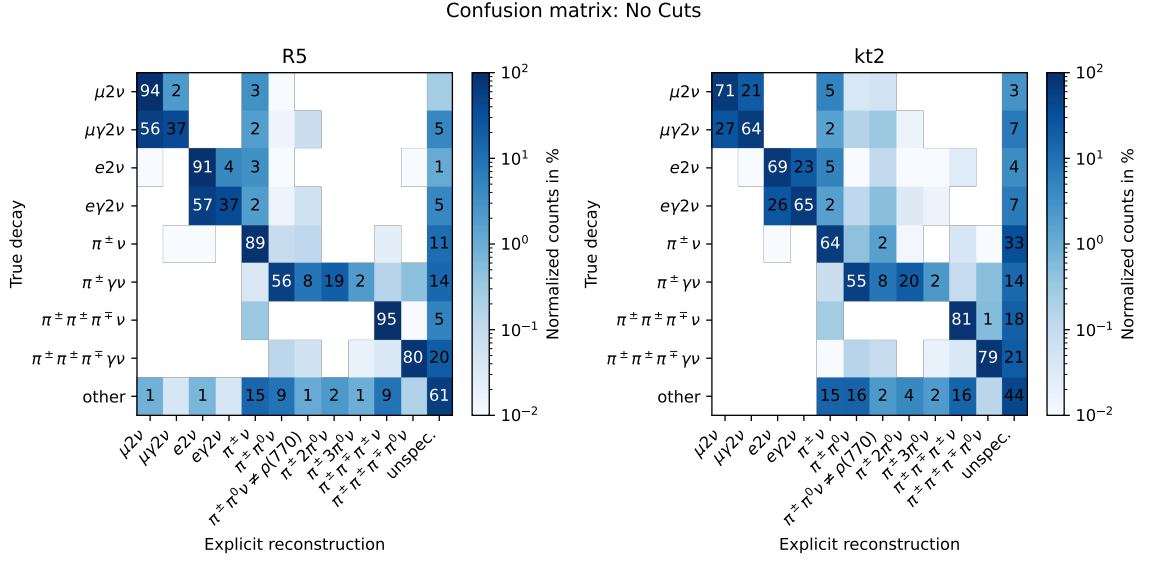


**Figure 5.3.:** Confusion matrices for the explicit reconstruction algorithms without any cuts applied. The confusion matrices show the normalized number of jets, stemming from a certain decay mode at the generator level ( $y$ -axis), being identified as a certain decay mode at the reconstruction level ( $x$ -axis).

**Table 5.1.:** Number of jets assigned a certain generator label for  $k_T2$  and  $R5$  jet clustering.

	$\mu 2\nu$	$\mu \gamma 2\nu$	$e 2\nu$	$e \gamma 2\nu$	$\pi^\pm \nu$	$\pi^\pm \gamma \nu$	$\pi^\pm \pi^\pm \pi^\mp \nu$	$\pi^\pm \pi^\pm \pi^\mp \gamma \nu$	$\Sigma$
$R5$	26212	6317	26916	6415	20601	77163	19010	10662	198770
$k_T2$	19641	5924	20235	5978	15889	77251	18991	10684	175420

The number of jets in the used dataset, in dependence on the generator label is shown in Table 5.1.

The jets are filtered to include only well-defined jets by applying cuts based on their properties. As a first step, it is useful to take a look at the jets, which are formed around the decay products. While in theory, the jets would form around the decay products of one of the  $\tau$  leptons each, the jets may also be malformed in practice. Two different cases can lead to such a situation. The first case arises if the products of a single  $\tau$  lepton are spread over multiple jets. The second case appears if products of both  $\tau$  leptons are clustered into a single jet. In both cases, the jets are not formed around the decay products of a single  $\tau$  lepton. To avoid such situations, the following cuts are applied to the jets:

1. The other jet in the event, which is the furthest away from the current jet, must be at least 3.0 rad away from the current jet.
2. The particle with the greatest separation from the jet axis may only be at most  $(\Delta R)^2 < 0.1$  away from the jet axis.

To evaluate the performance of this limitation the confusion matrices for the explicit

## 5. Evaluation of Reconstruction Algorithms

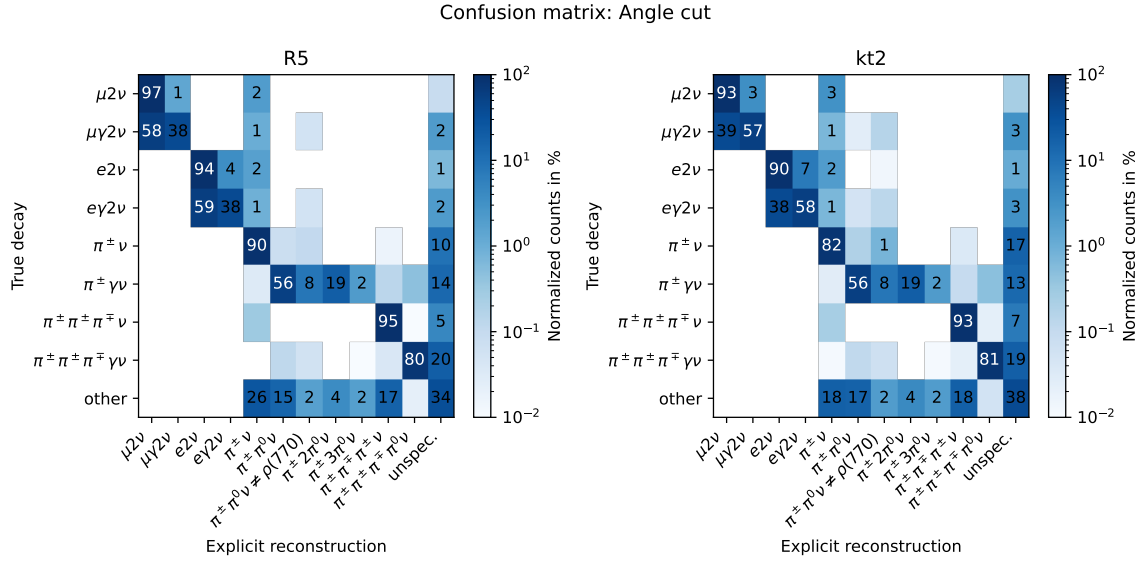


**Figure 5.4.:** Confusion matrices for the explicit reconstruction algorithms with the applied angle cuts on the jet properties. The confusion matrices show the normalized number of jets, stemming from a certain decay mode at the generator level ( $y$ -axis), being identified as a certain decay mode at the reconstruction level ( $x$ -axis).

reconstruction algorithms are shown in Figure 5.4. Furthermore, the distributions between the generated  $\tau$  and the reconstructed jet,  $\Delta\alpha$ , are shown in Figure 5.5. The calculation of this angle is explained in section 4.4.

This cut reduces the efficiency of the reconstruction algorithms to 90 % for R5 clustering

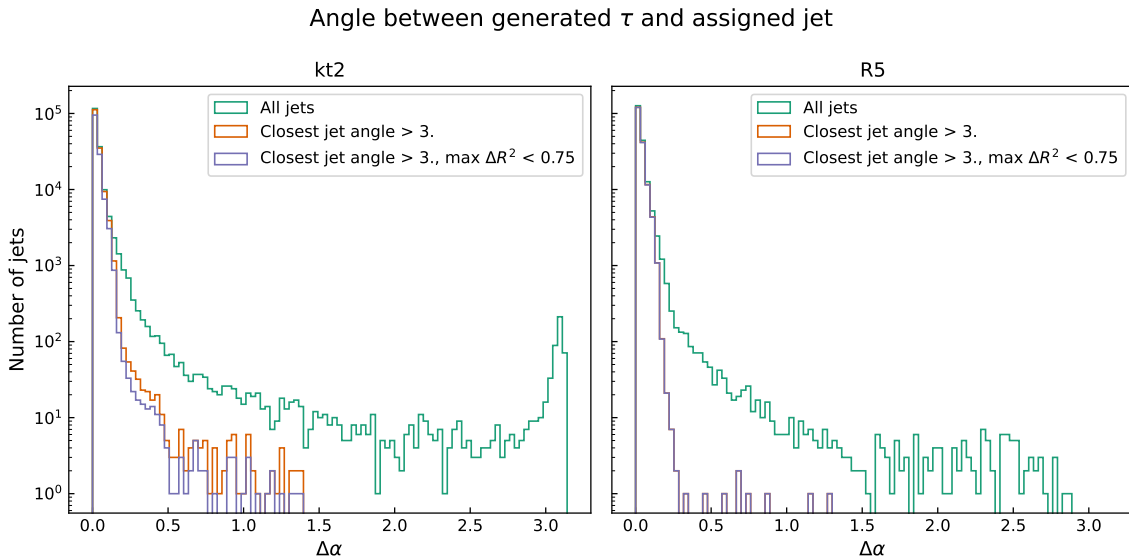


**Figure 5.5.:** Distributions of the angles between the generated  $\tau$  lepton and the closest reconstructed jet for each generated  $\tau$  lepton.



and 78 % for  $k_T2$ . On the other hand, the purity of the reconstruction algorithms is increased by a noticeable amount. This observation can be made when comparing Figure 5.3 and Figure 5.4. The confusion matrices shows a good match between the generated decay mode and the reconstructed decay mode. As this thesis also aims to evaluate the performance of explicit reconstruction at highest purities, further cuts are studied to reach this goal.

Motivated by the physics of  $\tau$  lepton decays, the following cuts are successively applied to the jets:

1. The total energy of the jet must be between 1.7 GeV and 45.6 GeV. The cut is motivated by the symmetrical decay of the Z boson into two  $\tau$  leptons. Since the two jets are assumed to be symmetric, the energy of the jets should also be symmetric, and thus the energy of the jets should be at not exceed half the mass of the Z boson [3].
2. The total charge of the jet may only be  $\pm 1$ . Again this follows from the fact, that we assume both of the jets to exactly contain the products of one of the  $\tau$  leptons.
3. The number of neutral hadrons in the jet should be zero. This cut is motivated by the explicit reconstructions implemented in this thesis, as the neutral hadrons are not part of any of the decay modes.
4. Finally to further exclude the effects of FSR, the number of photons in the jet should not be equal to one.

As multiple of those cuts may reduce the efficiency of the reconstruction by a large amount, the cuts are applied in a stepwise manner. To evaluate the reduction in efficiency as a function of jet energy, the distributions of the total jet energy for the jets versus the multiple constraints are presented in Appendix C, i.e. in section C.2. The largest influence on the

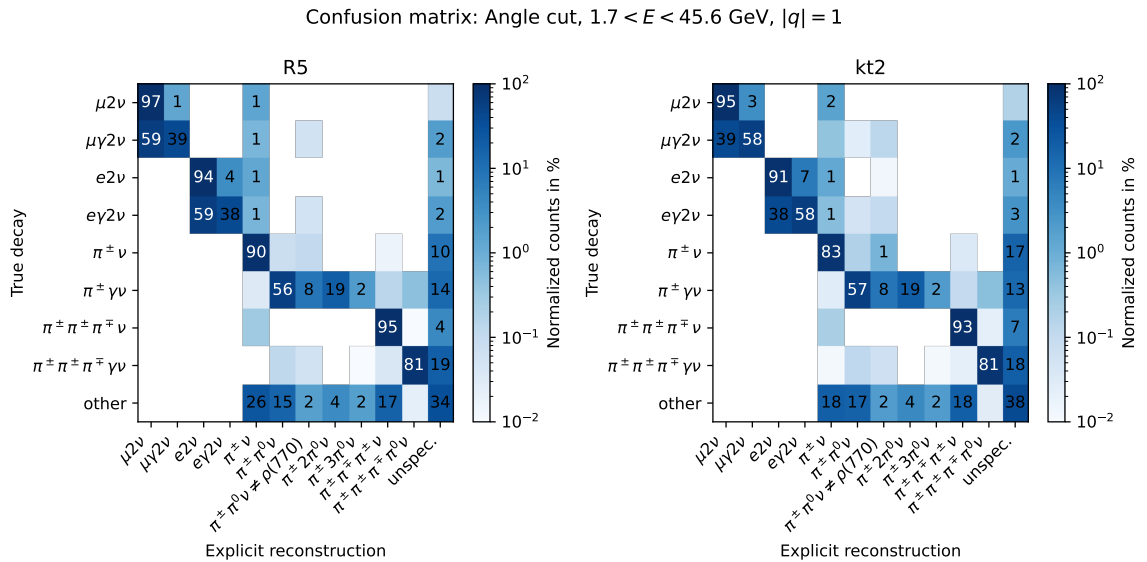


**Figure 5.6.:** Confusion matrices for the explicit reconstruction algorithms with the applied angle cuts on the jet properties and the additional cuts on the jet energy and charge.

energy spectrum of the jets arises from the cut on the angles between the jets, reducing the total number of accepted jets with an additional decrease on soft jets. This is expected as soft jets have the largest ratio of transverse momentum to total momentum. Secondly, the cut on the total jet energy has a minor influence on the flanks of the distribution. The cut on the total charge of the jet has a minor influence on the distribution, indicating that most jets are already correctly reconstructed, at least in terms of charge.

In addition, the most advanced statement on the purity after applying the cuts is formed after examining the confusion matrices for the explicit reconstruction algorithms. The confusion matrices for the application of the cuts on the jet energy, jet charge, and jet angles are displayed in Figure 5.6 and show increases in the purity of the leptonic decay modes compared to the angle cut itself. In the hadronic decay modes, no significant changes are observable.

Excluding jets containing neutral hadrons is motivated by the decay modes implemented in the thesis not allowing for neutral hadrons to be part of any of the reconstructions. With the generator labels in the analysis also being reduced to those not containing neutral hadrons leads to the question, of why any jets are excluded by this step. The main fraction for neutral hadrons occurring in the jets can be explained by quark pair production, following from FSR photons. In a full simulation of the detector behavior other sources of neutral hadrons, i.e. wrongly identified HCAL clusters, also may need to be considered. The confusion matrix after the application of this cut is shown in Figure 5.7. All hadronic decay modes of the  $\tau$  lepton benefit from the exclusion, with a notable increase of 1 % to 3 % in purity for those decays.

In the last step, the number of photons in the jets may only be zero or greater than one.

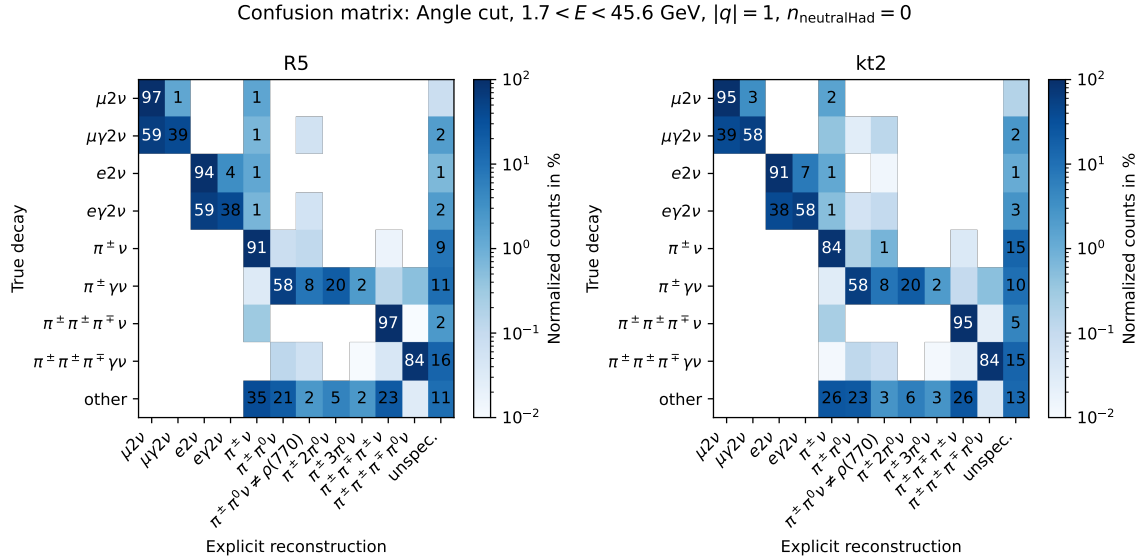


**Figure 5.7.:** Confusion matrices for the explicit reconstruction algorithms with the applied angle cuts on the jet properties and the additional cuts on the jet energy, charge and the number of neutral hadrons.

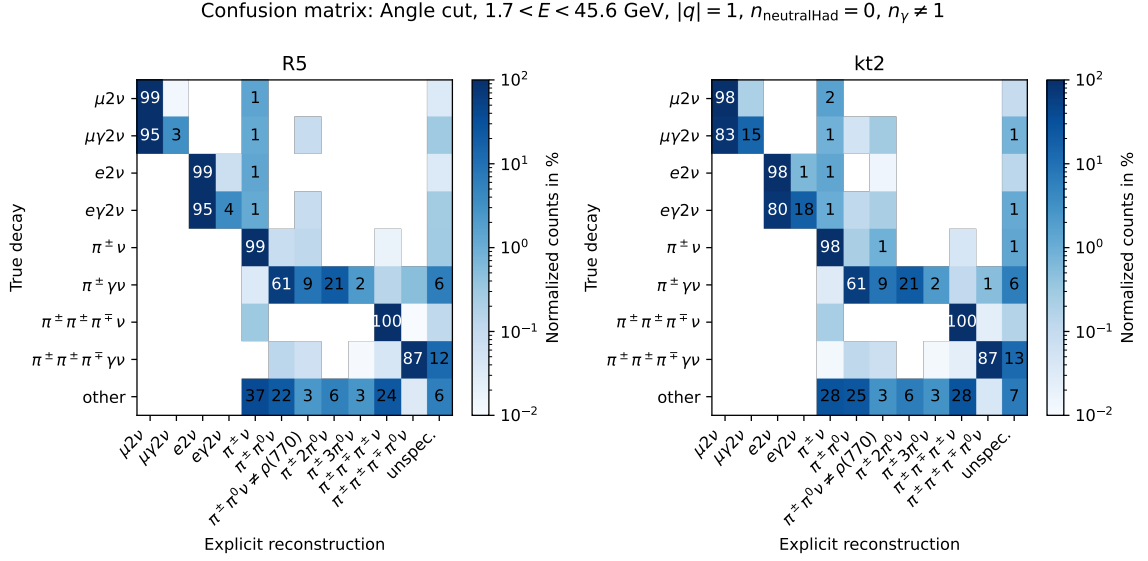


**Figure 5.8.:** Confusion matrices for the explicit reconstruction algorithms with the applied angle cuts on the jet properties and the additional cuts on the jet energy, charge, the number of photons and the number of neutral hadrons.

Reducing the allowed number of photons can help to exclude jets containing FSR photons. Eliminating these jets can contribute to increasing the purity of the decay modes involving hadrons. On the other hand, it is logical, that after this cut, the efficiency and general usability of the leptonic decay modes involving FSR directly, is reduced drastically. Applying this cut leads to the confusion matrices shown in Figure 5.8. The purity of the leptonic decay modes is increased further (except FSR modes), while the purity of the hadronic decay modes is promoted to a near-perfect identification.

### 5.2.1. Efficiency of the Cuts

To evaluate the reduction in accepted jets based on the cuts presented in the previous section, the cut efficiency  $\epsilon_{\text{cut}}$  is defined. It represents the ratio of jets that are accepted after the application of the cuts to the jets that are accepted before the application of the cuts.

$$\epsilon_{\text{cut}} = \frac{N_{\text{accepted}}}{N_{\text{total}}} \quad (5.1)$$

To separate the effects on the different decay modes, the efficiency is evaluated for the different decay classes defined in section 4.4. Furthermore, the total cut efficiency is evaluated. Due to the correct ratios between the MC simulated decay modes, the total cut efficiency is also representative of the efficiency of the cuts in real-world data. The efficiency of the cuts is shown in Figure 5.9.

In general, we can observe that the *R5* jet clustering shows greater efficiency after the

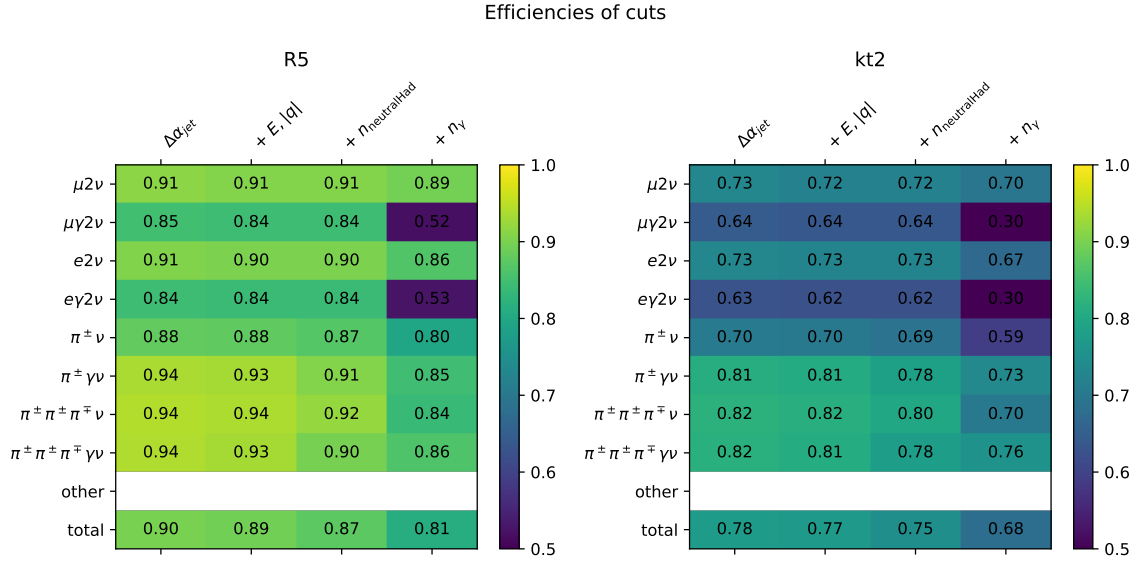


**Figure 5.9.:** Efficiency of the cuts applied to the jets for the explicit reconstruction algorithms. The efficiency is evaluated for the different decay classes defined in section 4.4.

application of the cuts<sup>1</sup>. The main reason behind this is the large number of parallel jets that arise using the  $k_T2$  algorithm. This effect can be observed the best when looking at the angular distributions in Figure 5.5. The smaller number of malformed jets in the R5 clustering leads to a higher efficiency after the application of the angular cuts on the jet spacing and spread. The cuts on energy and charge lead to a reduction in efficiency for all decay modes of around 1 % to 2 %. The largest effect on efficiency is promoted by the cut on the number of photons in the jet. It reduces the efficiency in the hadronic decays by 7 % and by 30 % in the leptonic decays involving FSR. This large reduction is expected, as the cut is not designed for those decays, but rather for improving the purity of the hadronic decays.

### 5.3. Exclusion of FSR

As explained in subsection 4.1.1 the photons created in the decay of the  $\tau$  lepton may be due to FSR. To evaluate a threshold value for the photon exclusion in jets, the distribution of the energy of the photons in the jets is evaluated. Especially the following comparison is of interest: The energy of the photons in the jets with exactly one photon is more likely to be produced by FSR than those in jets with more than one photon. For example, multi-photon jets can be caused by decaying intermediates such as the  $\pi^0$  meson. The distribution of the energy of the photons in the jets is shown in Figure 5.10. Based on this distribution a threshold of 200 MeV is chosen to exclude the photons from jets.

<sup>1</sup>No energy or mass cuts were applied to the R5 jets before these cuts.

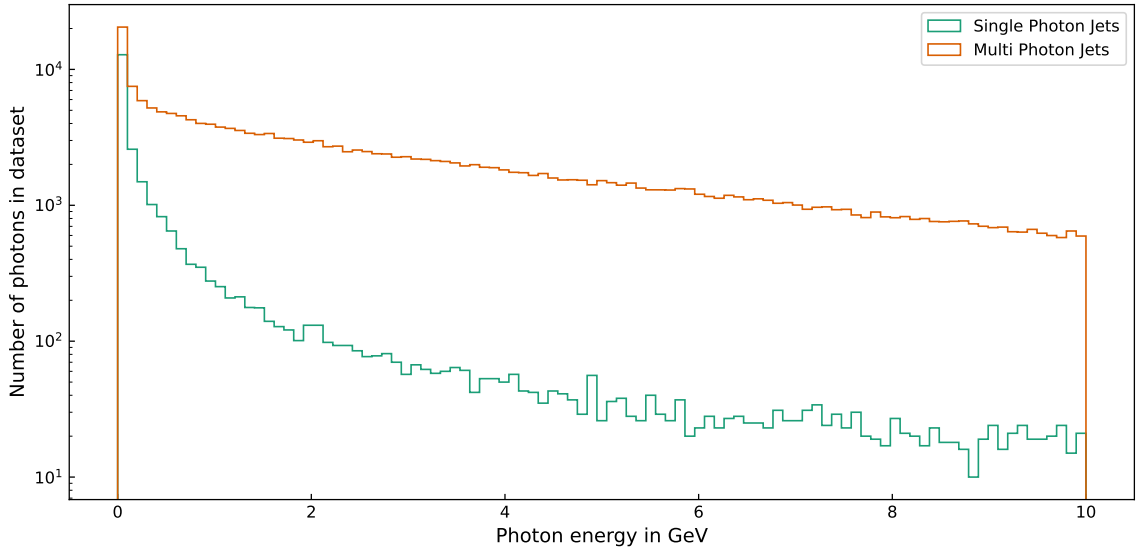


**Figure 5.10.:** Distribution of the energy of the photons in the jets for the explicit reconstruction algorithms. The distribution is evaluated for jets with exactly one photon and jets with more than one photon. The jets are created using  $k_T2$  clustering.

### 5.3.1. Evaluation of the $\pi^0$ Reconstruction

Based on the energy distribution we need to evaluate if the cut on the photon energy is too restraining. A measure for this can be estimated by the reconstruction of  $\pi^0$  candidates in the remaining jets using the method described in subsection 4.2.1. Comparing the baselines and shapes of the  $\pi^0$  mass distributions for the jets with and without the cut on the photon energy, the cut is evaluated. The distributions are shown in Figure 5.11. Additionally, a fit employing a Breit-Wigner distribution is employed to get an estimate for the mass width of the  $\pi^0$  meson. The fit is shown in section C.3. It is observable, that there is a slight reduction in the baseline of the  $\pi^0$  mass distribution for the jets with the cut on the photon energy. This reduction is expected, as the photons produced by FSR are excluded from the jets. Furthermore, the total height of the distribution is reduced, indicating a slight reduction in the efficiency of the  $\pi^0$  reconstruction. The width of the  $\pi^0$  mass distribution is not affected by the cut on the photon energy. The parameters obtained by the fit on the FSR cut distributions are also listed in the appendix.

### 5.3.2. Evaluation of the $\rho(770)^\pm$ Reconstruction

Using the very good reconstruction of the  $\pi^0$  meson, the reconstruction of intermediate  $\rho$  mesons can be studied quite easily, because of the very low limit for the non- $\rho$  decay  $\tau \rightarrow \pi^\pm \pi^0 \nu_\tau$  showing a branching ratio of  $(3.0 \pm 3.2) \times 10^{-3}$  [3]. We thus expect a large abundance of reconstructed  $\rho$  modes in  $\tau \rightarrow \pi^\pm \pi^0 \nu_\tau$  decays. Checking against the confusion matrices shows a four-to-one ratio of  $\rho$  to non- $\rho$  decays. This ratio indicates too harsh cuts

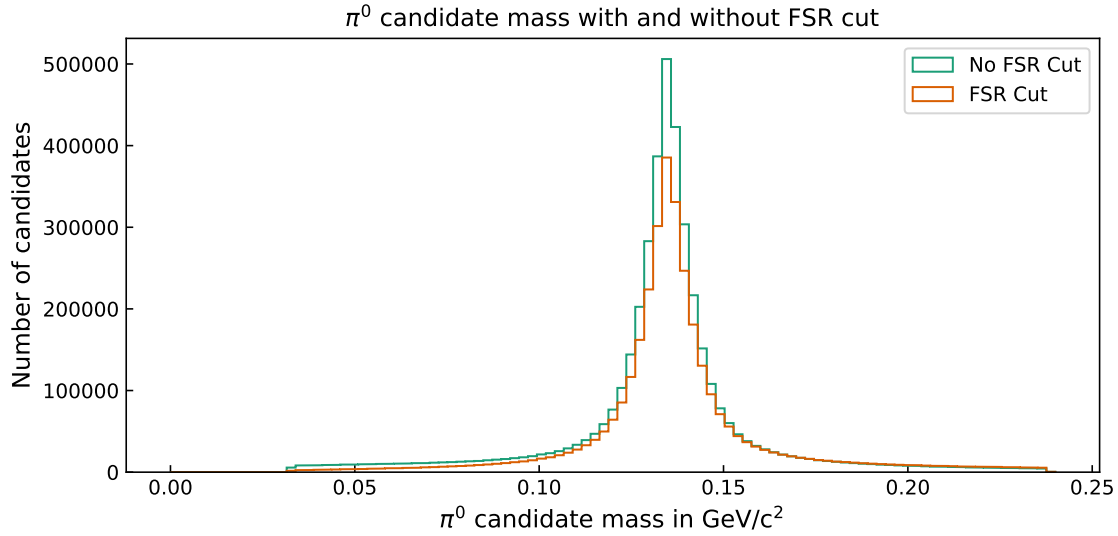


**Figure 5.11.:** Distribution of the reconstructed  $\pi^0$  masses for the jets with and without the cut on the photon energy. The jets are created using  $R5$  clustering.

on the  $\rho$  reconstruction. For better results in the  $\rho(770)^\pm$  domain, further steps would be needed. The  $\rho$  reconstruction is not further evaluated in this thesis.

## 5.4. Summary

Using the explicit reconstruction algorithms presented in this thesis, high efficiency is achieved with a correct mapping to the true decay in most cases, leading to a high purity of the tagged decay modes. In general, the rate of false tagging is very low, for fakes resulting from  $Z \rightarrow qq$  events and other sources. On the other hand, the importance of the jet definition for a good performance of the explicit reconstruction is shown. With simple cuts, the set of jets is already drastically refined. The need for good jet definition can also be used to study jet clustering algorithms and their impact on analyses like this. Finally, the exclusion of FSR photons shows only a small effect on the results, neither significantly increasing nor decreasing the performance in the identification of hadronic decay modes. As a consequence, other techniques to increase the purity of the hadronic decay modes, such as improving the rejection in the  $\pi^0$  reconstruction, can be explored.

Especially using the  $R5$  clustering method, a very good ratio of efficiency and tagging performance can be achieved, with the purity of the decay modes constantly being a few percent above the ones expressed by the  $k_{T2}$  clustering, as shown in figures 5.3 to 5.8. Especially as the efficiency of the  $R5$  clustered jets constantly outperforms the efficiency achieved using  $k_{T2}$  as discussed in subsection 5.2.1, with approximately 30 % incorrectly clustered jets by  $k_{T2}$  and only 10 % in the case of  $R5$ . From these observations, the conclusion follows, that  $R5$  or inclusive jets in general are the better choice than exclusive jets for explicit reconstruction.

## 6. Conclusion

### 6.1. Summary

For tagging the flavor of jets resulting from the decay of the  $Z$  boson, both ML algorithms employed in this thesis show acceptable performance depending on the physics space to cover. Both provide efficient  $\tau$ -jet tagging. However, the Particle Transformer Network model is shown to achieve better performance overall, especially with respect to quark jet separation. This underscores its position as the current state of the art for ML techniques in the field of jet tagging at collider experiments. With the FCC-ee on the horizon in the 2040s, the successors of this method could be valuable for experiments at the FCC-ee. Transformer-based networks represent a milestone in ML techniques and further developments in this area are likely to play a major role at the FCC-ee.

For the task of identifying jet flavors, the  $k_T2$  algorithm proves to be an intuitive and physically motivated choice. With its slightly modified methodology, the  $R5$  algorithm yields very good performance. The  $R5$  algorithm is especially useful when the decay mode of the  $\tau$  is of interest, as using it allows for very good separation in an explicit reconstruction approach. Depending on the cuts applied and the observed decay mode, rates of correct identification between 80 % and more than 99 % are achievable. Especially the ratio of purity and efficiency beats the ones achieved using  $k_T2$  clustering. Furthermore, it is shown, that explicit reconstruction algorithms on a jet level – at least in the implementation used – require the most suitable jet clustering algorithms to be used, for achieving the best performance possible. Additionally, an important aspect of the explicit reconstruction is the goal of the analysis, as the performance of the algorithms can vary greatly depending on the specific goal and thus limit the universality of a certain implementation. On the other hand, this limitation can also provide opportunities for finer control in analysis, not available with other methods, like ML. Especially the ability to separate specific decay modes of interest, or focus on specific particles in the decay chain, can be a promising idea to explore in the analysis of real data.

### 6.2. Potential Future Work

At this early stage of studying  $\tau$  decays at the IDEA detector in the context of the FCC-ee, there are many opportunities for future work. The performance of the ML algorithms, but also the explicit reconstruction algorithms, is highly dependent on the quality of the input data. While a DELPHES simulation provides very good performance at this early stage, where

full simulation of all detector components of the IDEA detector is not yet available, it remains to be seen if the performance of the algorithms will be as good when using the results from a full simulation. In particular, the gamma separation and the identification of  $\pi^0$  mesons are expected to be more challenging in a full simulation. However, there may be other opportunities for improvement, for example by using the calorimeter information available in the full simulation to improve the performance of the algorithms. Doing such a full-simulation-study would be a valuable asset for the IDEA collaboration, as it would provide better insights into the performance of the algorithms in a more realistic environment.

For the explicit reconstruction algorithms, there are multiple ways to achieve improvements in performance and universality. One way would be to implement further decay modes and classifications in the current framework and style of the algorithms. Especially focussing on the separation of Kaons and Pions could be a worthwhile next step for the analysis of the  $\tau$  decay modes. In a final step, the algorithms could then be transferred to the FCCAnalyses framework[21], which is the standard source of the CERN for the analysis of FCC data.

Another approach at improving the explicit reconstruction algorithms would be to move from a jet-based approach to an event-based approach, leveraging all the information available in the event at once and overcoming obstacles imposed, due to suboptimal jet clusterings. The large combinatorics involved in such an approach would require a more sophisticated approach, such as using event-level likelihood trees, to achieve good performance. Additionally or alternatively, ML techniques could be used to tag the decay mode of  $\tau$  leptons at FCC-ee. Especially taking the to-be-expected improvements in computational power in the next decades into account, this could be a very promising approach to achieve very good performance in the tagging of  $\tau$  decay modes.



# Bibliography

- [1] *The Standard Model*. CERN. Apr. 29, 2024. URL: <https://home.cern/science/physics/standard-model> (visited on 05/24/2024).
- [2] Michael Krämer. “The Standard Model of Particle Physics”. *Phenomenology of the Standard Model* (4/4). July 11, 2017. URL: <https://indico.cern.ch/event/632201/>.
- [3] R. L. Workman et al. “Review of Particle Physics”. In: *PTEP* 2022 (2022), p. 083C01. DOI: 10.1093/ptep/ptac097.
- [4] Mogens Dam. *Tau-Lepton Physics at the FCC-ee Circular  $e^+e^-$  Collider*. Dec. 17, 2018. DOI: 10.48550/arXiv.1811.09408. arXiv: 1811.09408 [hep-ex, physics:hep-ph]. URL: <http://arxiv.org/abs/1811.09408> (visited on 05/24/2024). Pre-published.
- [5] *ATLAS Measures Symmetry of Higgs Boson Decays to Tau Leptons*. ATLAS. June 20, 2024. URL: <https://atlas.cern/updates/briefing/Higgs-tau-symmetry> (visited on 07/22/2024).
- [6] *The Future Circular Collider*. CERN. Apr. 29, 2024. URL: <https://home.cern/science/accelerators/future-circular-collider> (visited on 05/24/2024).
- [7] Markus Klute. “Future Circular Collider Project”. Future Collider @ CERN - German Community Workshop (Bonn). May 23, 2024. URL: <https://indico.desy.de/event/44074/timetable/>.
- [8] A. Abada et al. “FCC-ee: The Lepton Collider”. In: *The European Physical Journal Special Topics* 228.2 (June 1, 2019), pp. 261–623. ISSN: 1951-6401. DOI: 10.1140/epjst/e2019-900045-4. URL: <https://doi.org/10.1140/epjst/e2019-900045-4> (visited on 05/24/2024).
- [9] Juska Pekkanen. “Noble Liquid Calorimetry for Future Collider Experiments”. Second ECFA Workshop on  $e^+e^-$  Higgs/EW/Top Factories (Paestum). Oct. 11, 2023. URL: <https://agenda.infn.it/event/34841>.
- [10] Federica Cuna et al. *Simulation of Particle Identification with the Cluster Counting Technique*. May 14, 2021.
- [11] Veronica Ilardi et al. “Compression and Thermal Conductivity Tests of Cryogel® Z for Use in the Ultra-Transparent Cryostats of FCC Detector Solenoids”. In: *IOP Conference Series: Materials Science and Engineering* 756 (June 30, 2020), p. 012005. DOI: 10.1088/1757-899X/756/1/012005.
- [12] William Frass and Roman Walczak. *Particle Detectors*. Oxford: Department of Physics at Oxford University, 2009. 38 pp. URL: <https://www2.physics.ox.ac.uk/sites/default/files/Detectors.pdf>.

- [13] David G. Charlton. “Tau Lepton Lifetime and Decay Branching Ratio Measurements at LEP”. In: *28th Rencontres de Moriond: Electroweak Interactions and Unified Theories*. 1993, pp. 349–356.
- [14] A Lusiani. “Tau Decays at the B-factories”. In: (2008).
- [15] The Belle Collaboration et al. “Measurement of the Tau Michel Parameters  $\bar{\eta}$  and  $\xi\kappa$  in the Radiative Leptonic Decay  $\tau^- \rightarrow \ell^- \nu_\tau \bar{\nu}_\ell \gamma$ ”. In: *Progress of Theoretical and Experimental Physics* 2018.2 (Feb. 1, 2018). ISSN: 2050-3911. DOI: 10.1093/ptep/pty003. arXiv: 1709.08833 [hep-ex]. URL: <http://arxiv.org/abs/1709.08833> (visited on 07/10/2024).
- [16] Alain Blondel. “Future Circular Colliders - FCC-ee” (DESY). 2009. URL: [https://physikseminar.desy.de/sites2009/site\\_physikseminar/content/e408/e75/e277497/e277522/e277524/Blondel\\_slides.pdf](https://physikseminar.desy.de/sites2009/site_physikseminar/content/e408/e75/e277497/e277522/e277524/Blondel_slides.pdf).
- [17] Spandan Mondal and Luca Mastrolorenzo. *Machine Learning in High Energy Physics: A Review of Heavy-Flavor Jet Tagging at the LHC*. Apr. 1, 2024. DOI: 10.48550/arXiv.2404.01071. arXiv: 2404.01071 [hep-ex, physics:physics]. URL: <http://arxiv.org/abs/2404.01071> (visited on 06/10/2024). Pre-published.
- [18] Christian Bierlich et al. *A Comprehensive Guide to the Physics and Usage of PYTHIA 8.3*. Mar. 22, 2022. DOI: 10.48550/arXiv.2203.11601. arXiv: 2203.11601 [hep-ex, physics:hep-ph]. URL: <http://arxiv.org/abs/2203.11601> (visited on 06/10/2024). Pre-published.
- [19] The DELPHES 3 collaboration et al. “DELPHES 3: A Modular Framework for Fast Simulation of a Generic Collider Experiment”. In: *Journal of High Energy Physics* 2014.2 (Feb. 2014), p. 57. ISSN: 1029-8479. DOI: 10.1007/JHEP02(2014)057. URL: [http://link.springer.com/10.1007/JHEP02\(2014\)057](http://link.springer.com/10.1007/JHEP02(2014)057) (visited on 07/10/2024).
- [20] Key4hep/EDM4hep. Key4hep: Turnkey Software for Future Colliders, July 8, 2024. URL: <https://github.com/key4hep/EDM4hep> (visited on 07/10/2024).
- [21] HEP-FCC/FCCAnalyses. FCC, July 8, 2024. URL: <https://github.com/HEP-FCC/FCCAnalyses> (visited on 07/10/2024).
- [22] Matteo Cacciari, Gavin P. Salam, and Gregory Soyez. “FastJet User Manual”. In: *The European Physical Journal C* 72.3 (Mar. 16, 2012), p. 1896. ISSN: 1434-6052. DOI: 10.1140/epjc/s10052-012-1896-2. URL: <https://doi.org/10.1140/epjc/s10052-012-1896-2> (visited on 07/10/2024).
- [23] Stefano Catani and Dieter Zeppenfeld. “Jet Algorithms”. In: (July 31, 2019). URL: <https://s3.cern.ch/inspire-prod-files-6/6904a3576c84c5d1f05a1f171cac3695> (visited on 06/10/2024).
- [24] Florian Beaudette. *The CMS Particle Flow Algorithm*. Jan. 31, 2014. DOI: 10.48550/arXiv.1401.8155. arXiv: 1401.8155 [hep-ex, physics:physics]. URL: <http://arxiv.org/abs/1401.8155> (visited on 06/10/2024). Pre-published.

- 
- [25] Jason Ansel et al. “PyTorch 2: Faster Machine Learning through Dynamic Python Bytecode Transformation and Graph Compilation”. In: *29th ACM International Conference on Architectural Support for Programming Languages and Operating Systems, Volume 2 (ASPLOS '24)*. ACM, Apr. 2024. DOI: 10.1145/3620665.3640366. URL: <https://pytorch.org/assets/pytorch2-2.pdf>.
  - [26] Huilin Qu, Congqiao Li, and Sitian Qian. *Particle Transformer for Jet Tagging*. Jan. 29, 2024. DOI: 10.48550/arXiv.2202.03772. arXiv: 2202.03772 [hep-ex, physics:hep-ph, physics:physics]. URL: <http://arxiv.org/abs/2202.03772> (visited on 04/09/2024). Pre-published.
  - [27] Huilin Qu. *Hqcms/Weaver-Core*. Mar. 6, 2024. URL: <https://github.com/hqcms/weaver-core> (visited on 04/09/2024).
  - [28] Torben Ferber. “Modern Experimental Physics 3 - (Astro)Particle Physics: Lecture 4”. Lecture (Karlsruhe). May 15, 2024.
  - [29] *Classification: ROC Curve and AUC | Machine Learning*. Google for Developers. URL: <https://developers.google.com/machine-learning/crash-course/classification/roc-and-auc> (visited on 06/14/2024).



## A. Distributions of the Variables Used in the Analysis

This section shows the distributions of the variables used in the analysis, displayed in Figure A.1 to Figure A.3. On the left side of the plots, the distributions are shown for the signal and background samples in comparison. The right side of the plot shows either the distributions within the  $Z \rightarrow \tau\tau$  grouped by particle type or the distributions of the total number of particles in the jet.

For a description of the variables see Table 2.2 in section 2.2.

## A. Distributions of the Variables Used in the Analysis

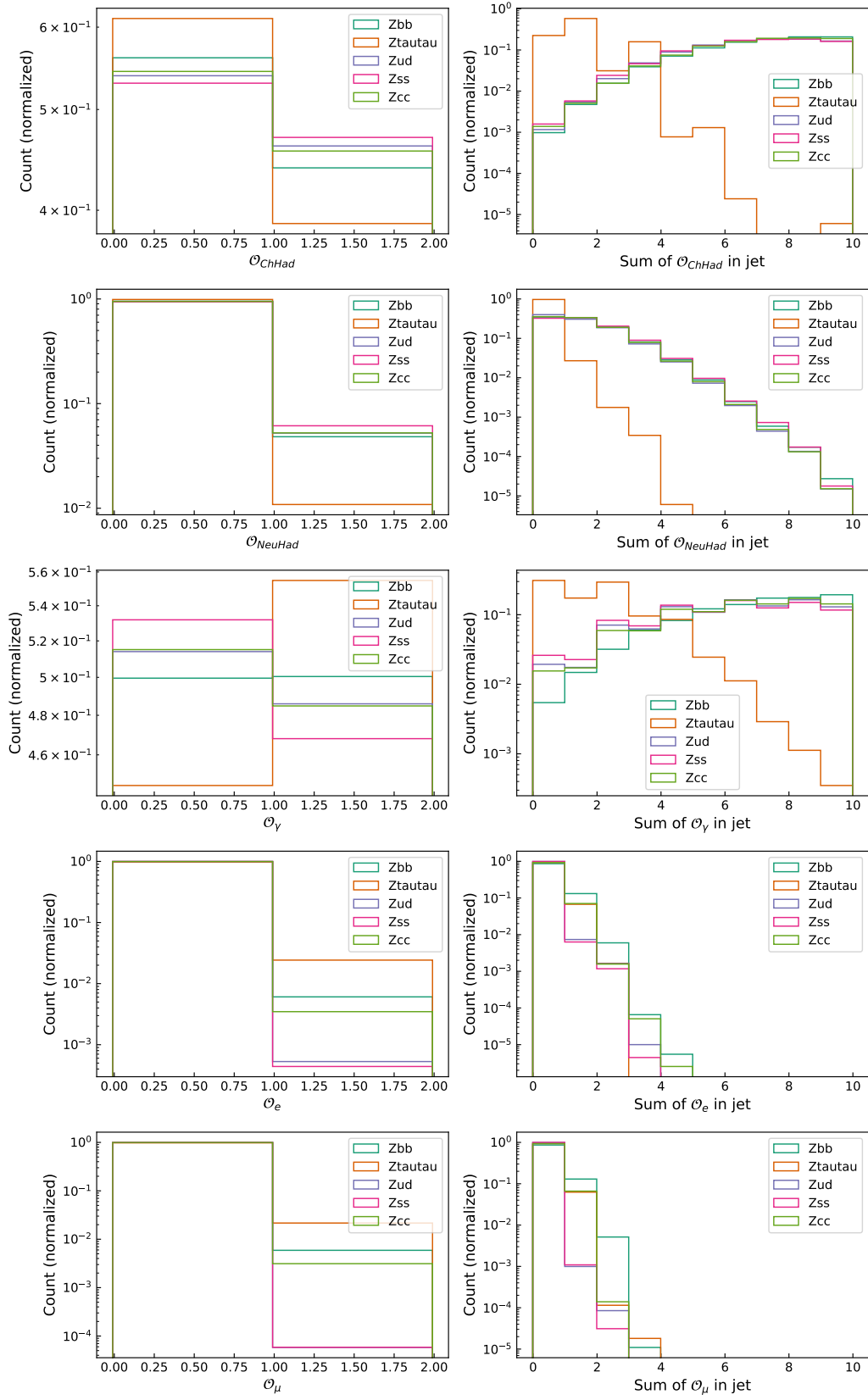


**Figure A.1.:** Distributions of the variables used in the analysis. (1/3)

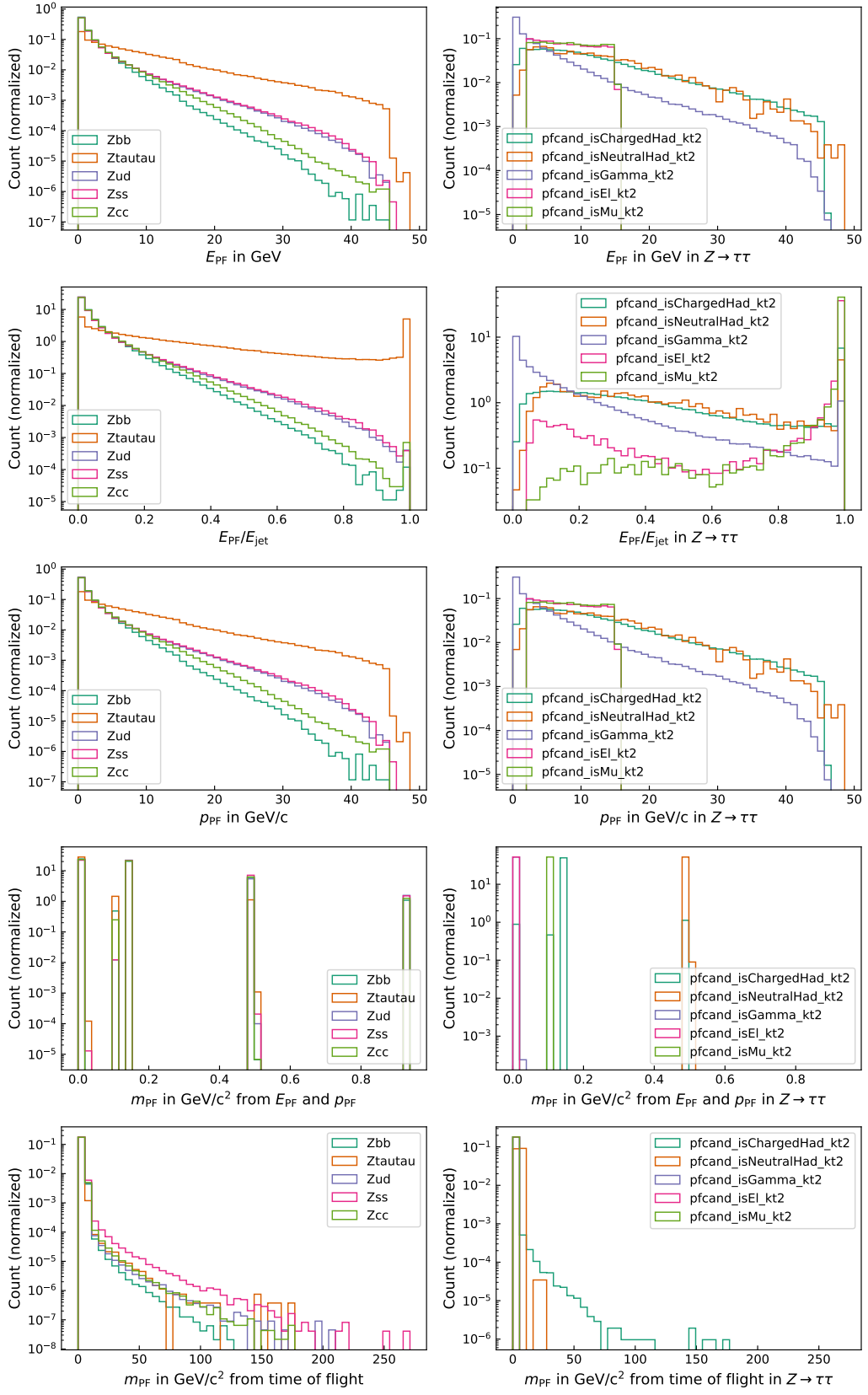


**Figure A.2.:** Distributions of the variables used in the analysis. (2/3)

## A. Distributions of the Variables Used in the Analysis

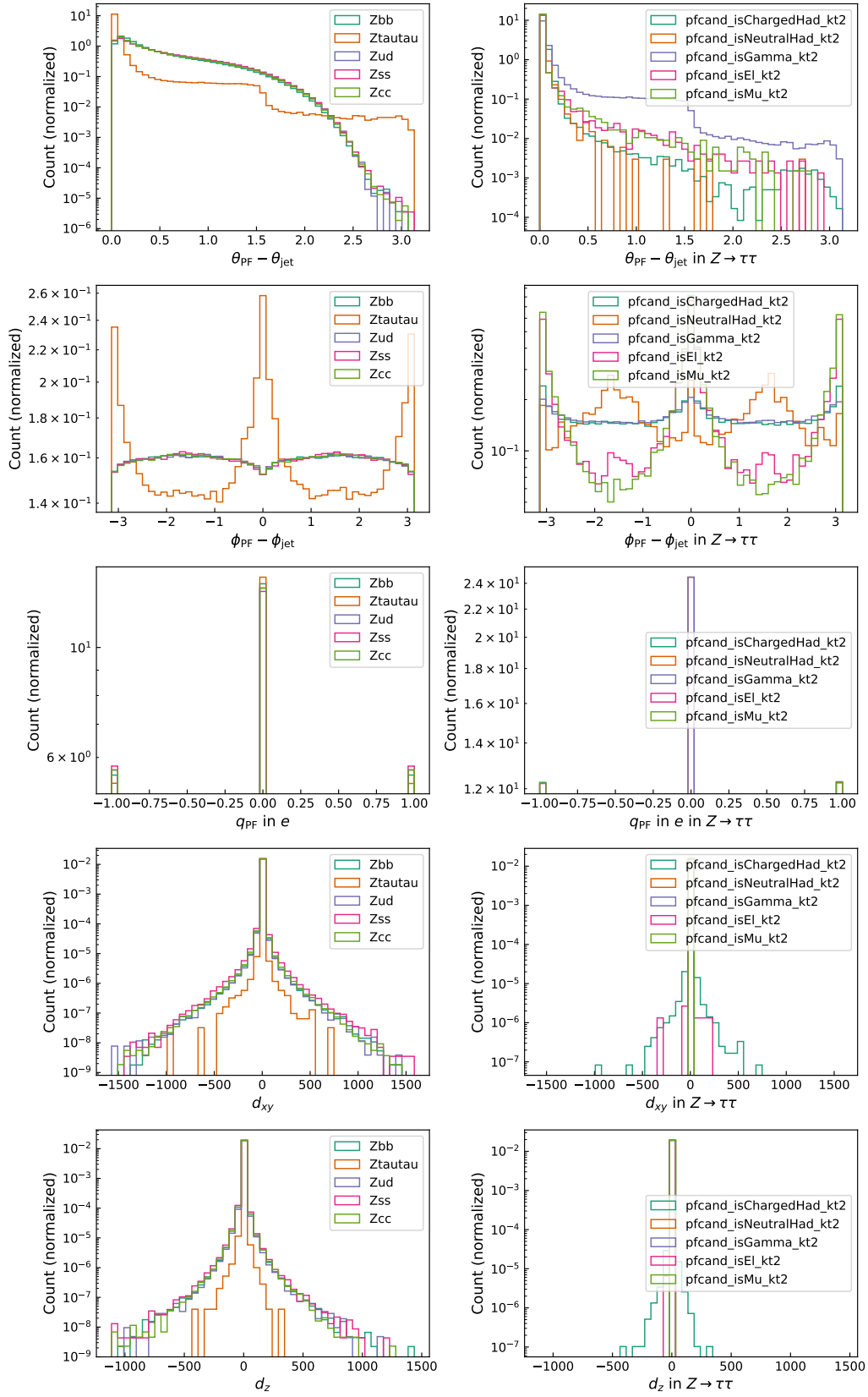


**Figure A.3.:** Distributions of the variables used in the analysis. (3/3)



## B. Independent Evaluation of ML-Models for Classification of $Z \rightarrow qq$ Jets

### B.1. ROC Curves for $Z \rightarrow qq$ Jets

Using ML models and methods from chapters 2 and 3, model performance on tagging jets from  $Z \rightarrow qq$  decays is evaluated. Figures B.1 and B.2 show the ROC curves of the SimpleNN model. Particle Transformer performance is shown in Figure B.3 and Figure B.4.

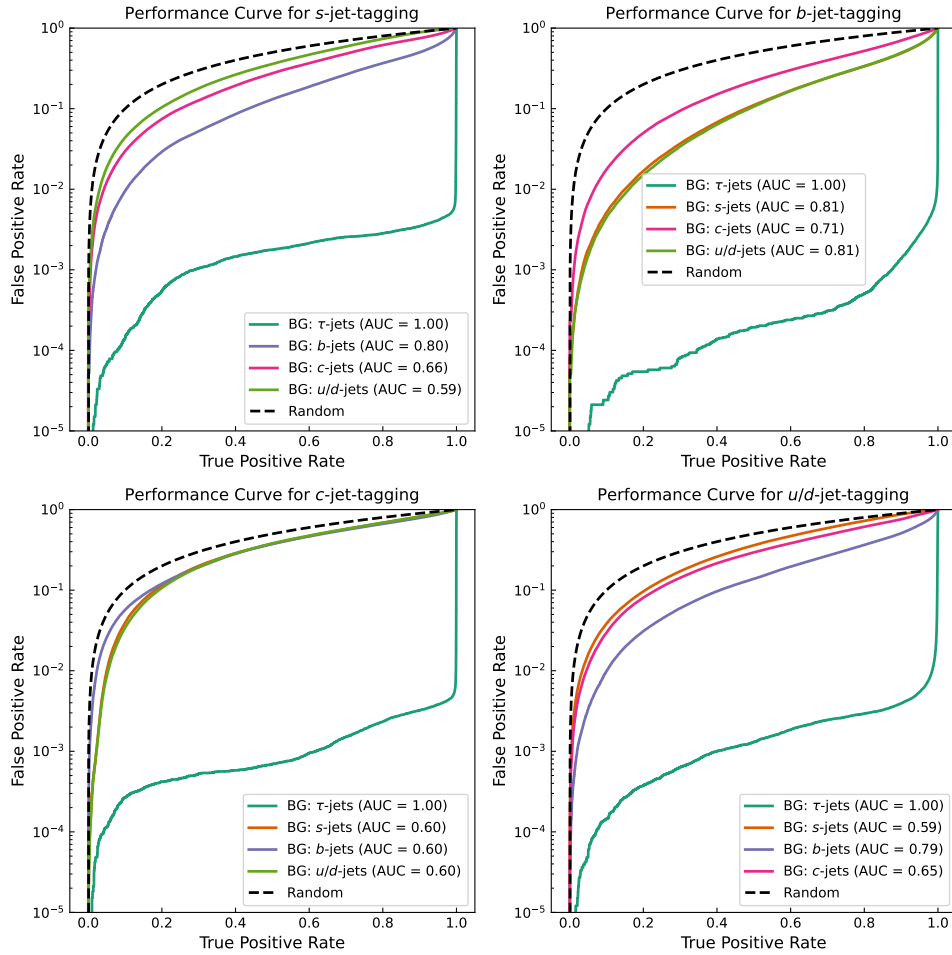


**Figure B.1.:** ROC curve of the SimpleNN model for the classification of  $Z \rightarrow qq$  jets. Input features: KIN+PID.

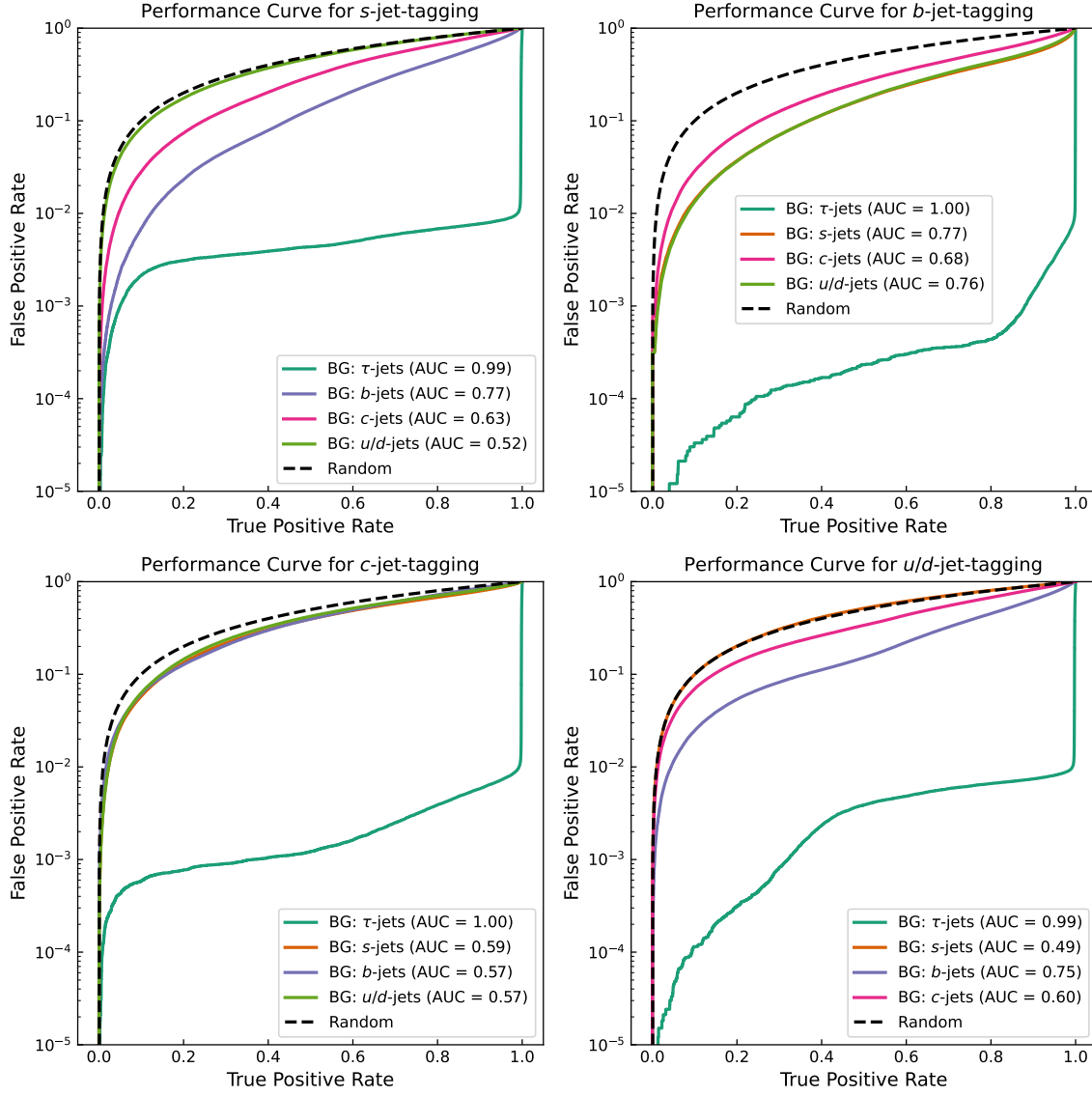


**Figure B.2.:** ROC curve of the SimpleNN model for the classification of  $Z \rightarrow qq$  jets. Input features: KIN.

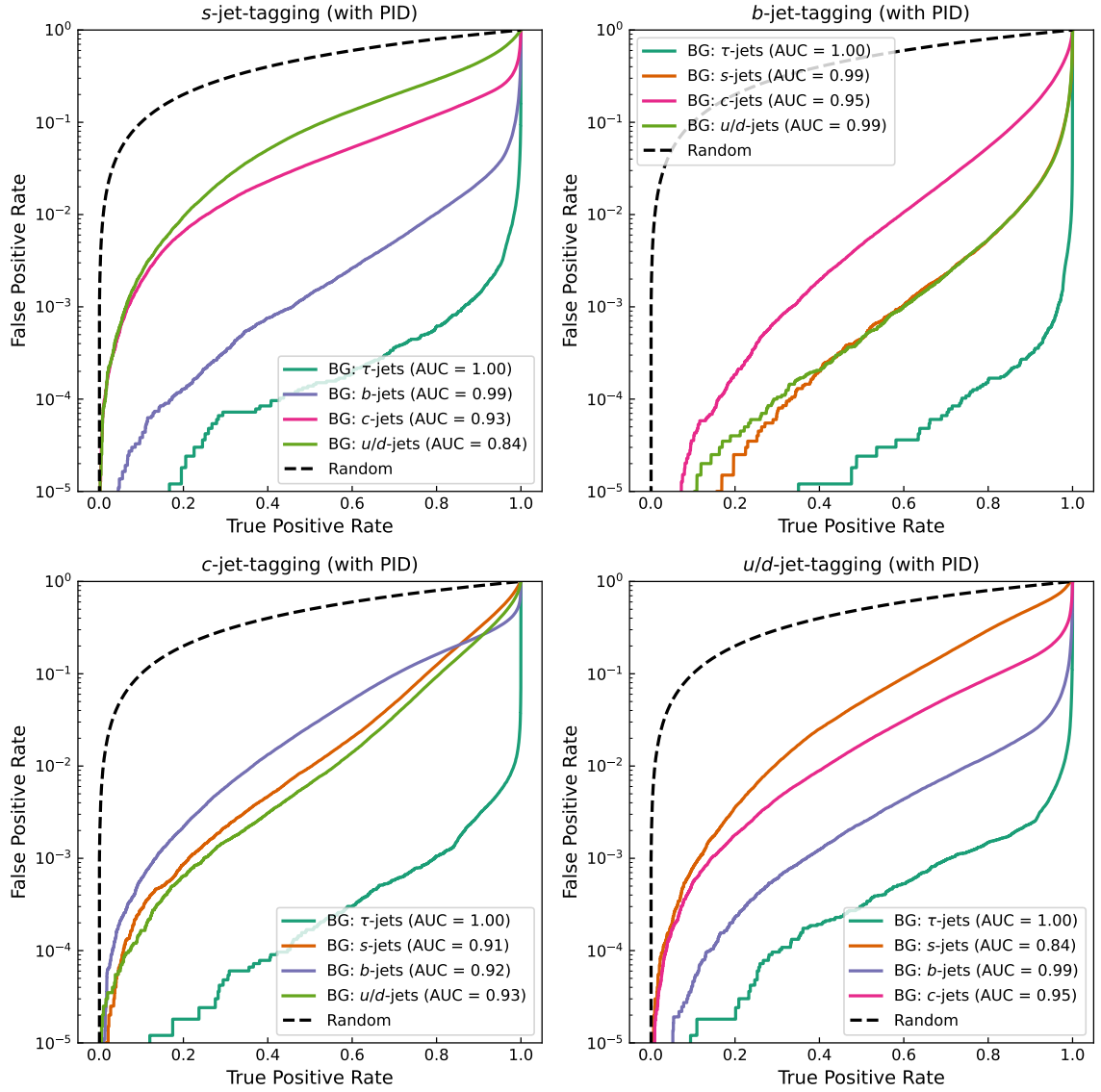


**Figure B.3.:** ROC curve of the Particle Transformer model for the classification of  $Z \rightarrow qq$  jets. Input features: KIN+PID.

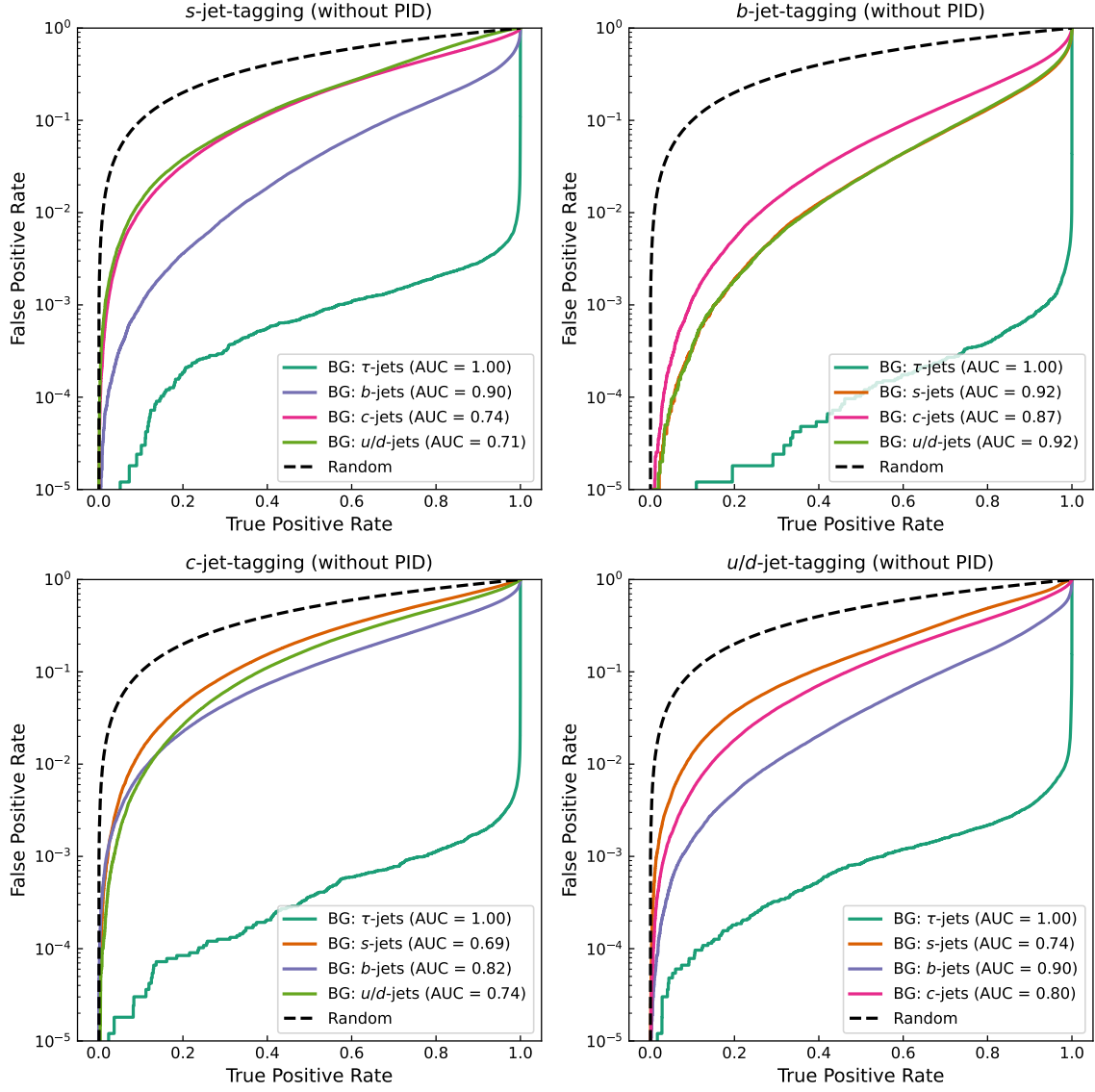


**Figure B.4.:** ROC curve of the Particle Transformer model for the classification of  $Z \rightarrow qq$  jets. Input features: KIN.

## B.2. Purity and Efficiency for $Z \rightarrow qq$ Jets

The performance of the models was evaluated using the ROC curves in the previous section. In this section the purity and efficiency of the models are shown. The purity and efficiency are shown for the SimpleNN model in Figure B.5 and Figure B.6 and for the Particle Transformer in Figure B.7 and Figure B.8. For normalization of the purity and efficiency the branching ratio of the  $Z$  decay is used as explained in subsection 3.1.1.

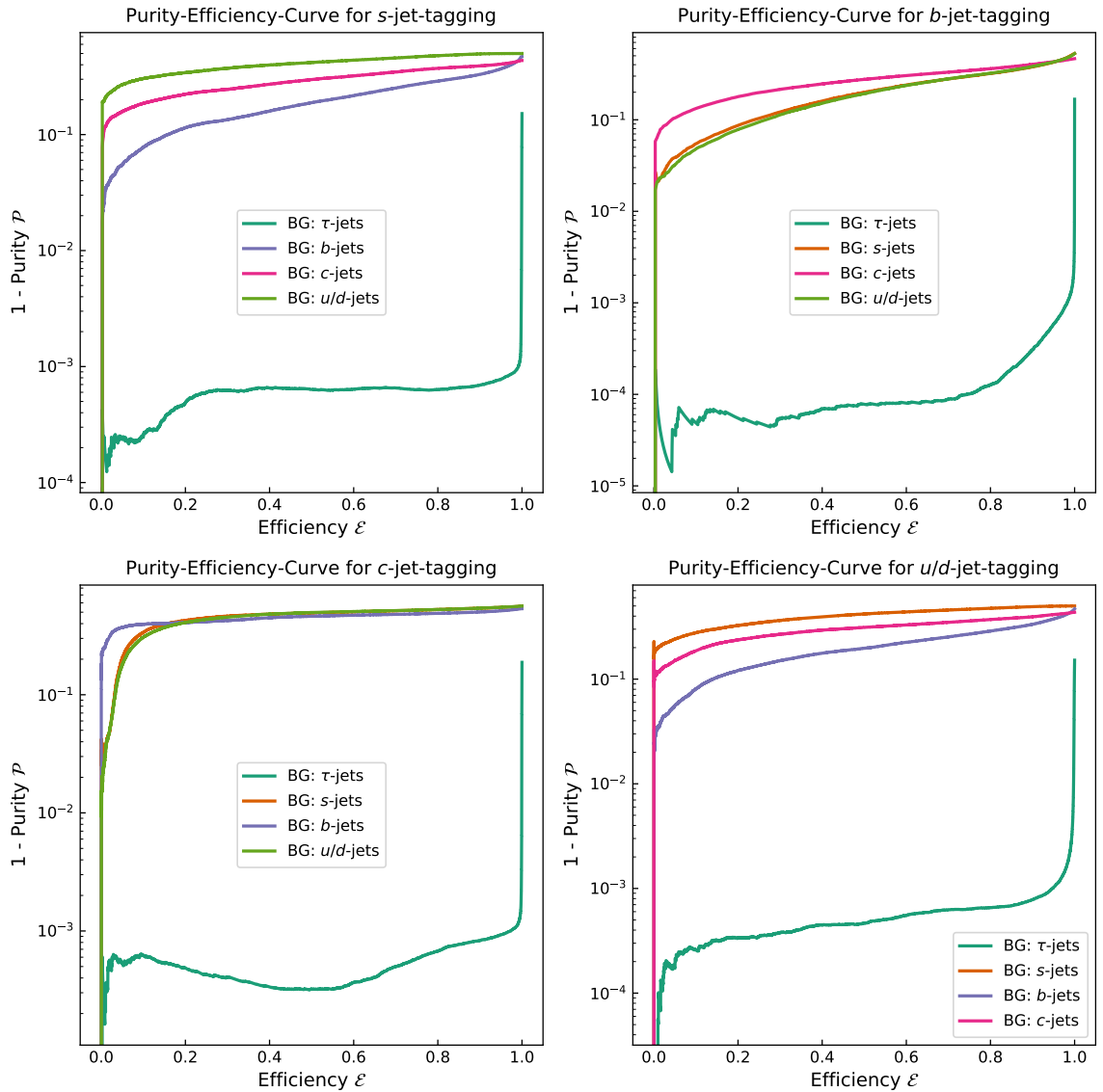


**Figure B.5.:** Purity and efficiency curve of the SimpleNN model for the classification of  $Z \rightarrow qq$  jets. Input features: KIN+PID.

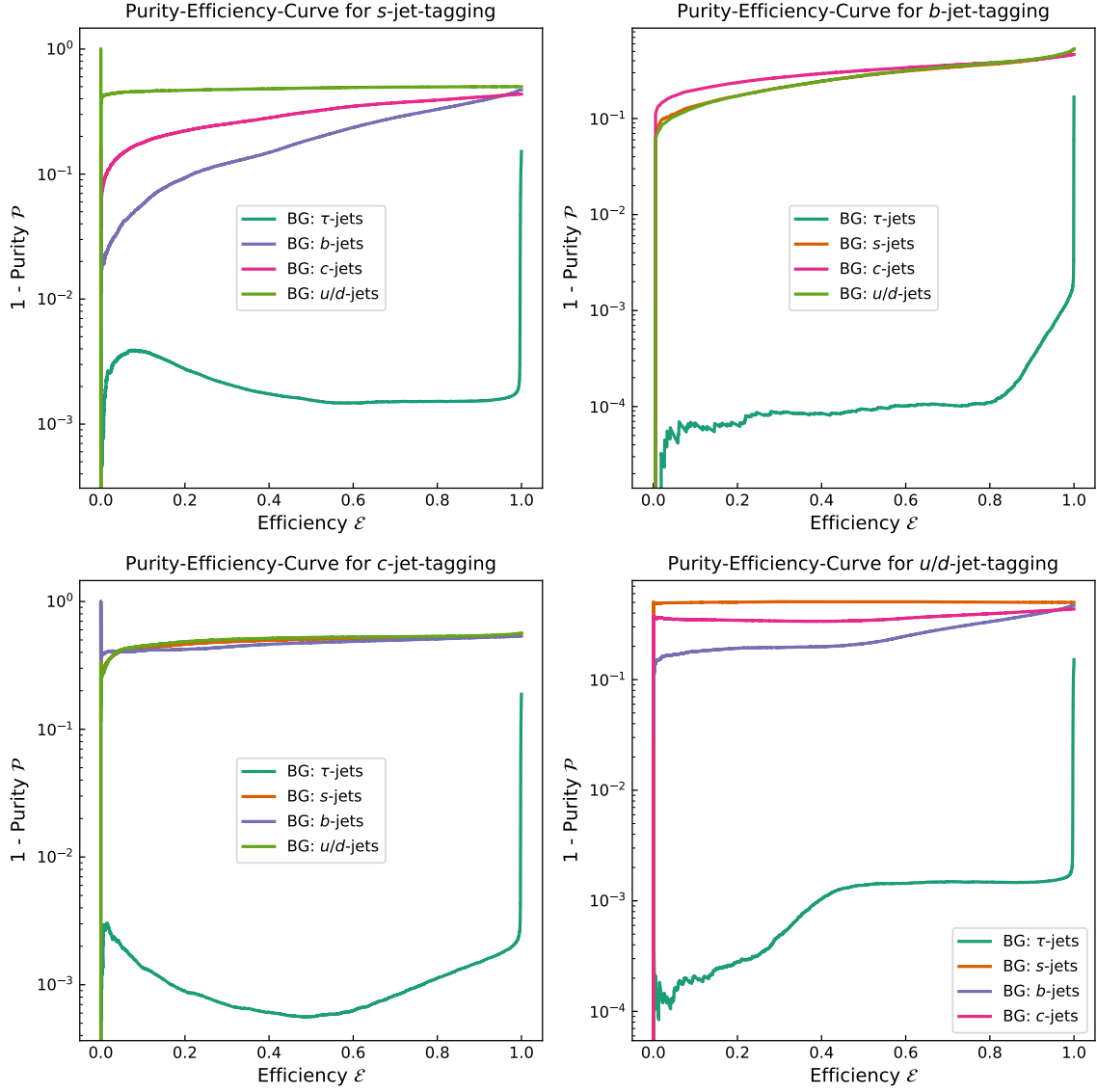


**Figure B.6.:** Purity and efficiency curve of the SimpleNN model for the classification of  $Z \rightarrow qq$  jets. Input features: KIN.

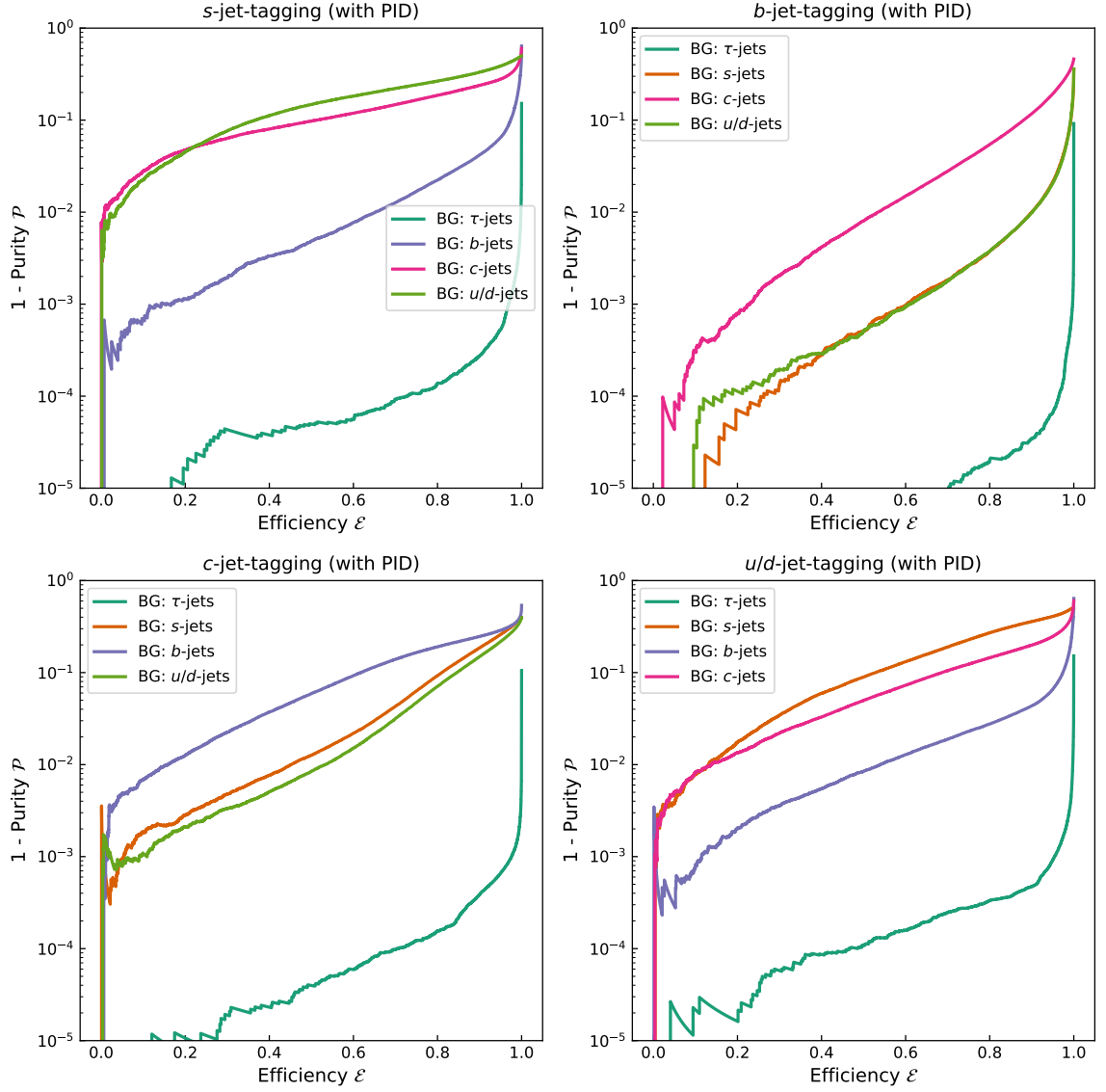


**Figure B.7.:** Purity and efficiency curve of the Particle Transformer model for the classification of  $Z \rightarrow qq$  jets. Input features: KIN+PID.

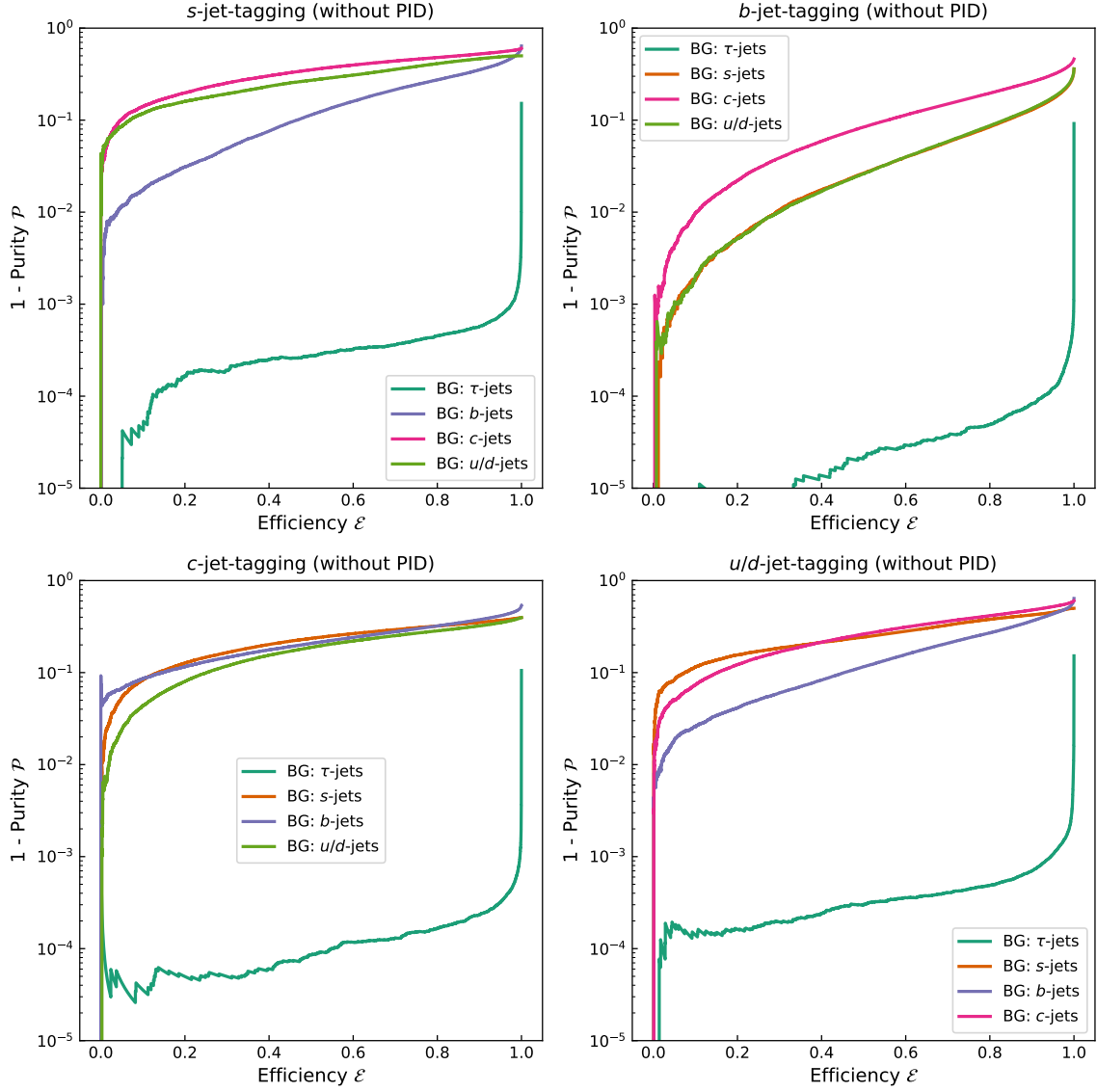


**Figure B.8.:** Purity and efficiency curve of the Particle Transformer model for the classification of  $Z \rightarrow qq$  jets. Input features: KIN.



## C. Detailed Analysis of the Explicit Reconstruction Performance

### C.1. Raw Jet Tagging Performance

The results for jet flavor identification using the explicit reconstruction algorithms presented in chapter 4 without the application of any jet-property-limiting cuts is displayed in Figure C.1. Except for the cuts, that are applied the methods are analogous to the ones in section 5.1.

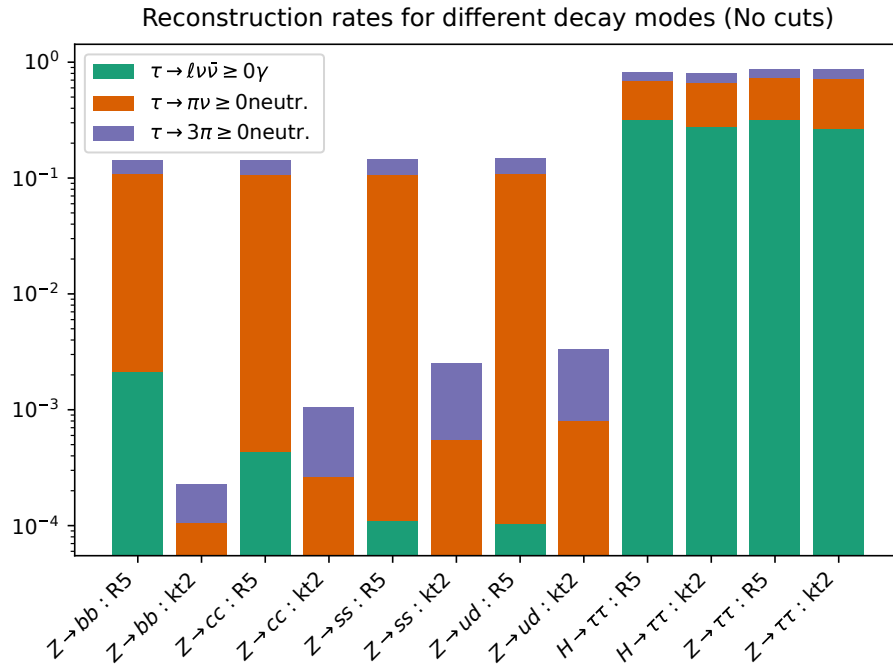


**Figure C.1.:** Jet flavor tagging performance using explicit reconstruction techniques without the application of cuts on the jet properties.

### C.2. Jet Energy Distributions

For assessing the effects of the multiple cuts applied to the dataset, the distribution of the total jet energy is shown in the following plots.

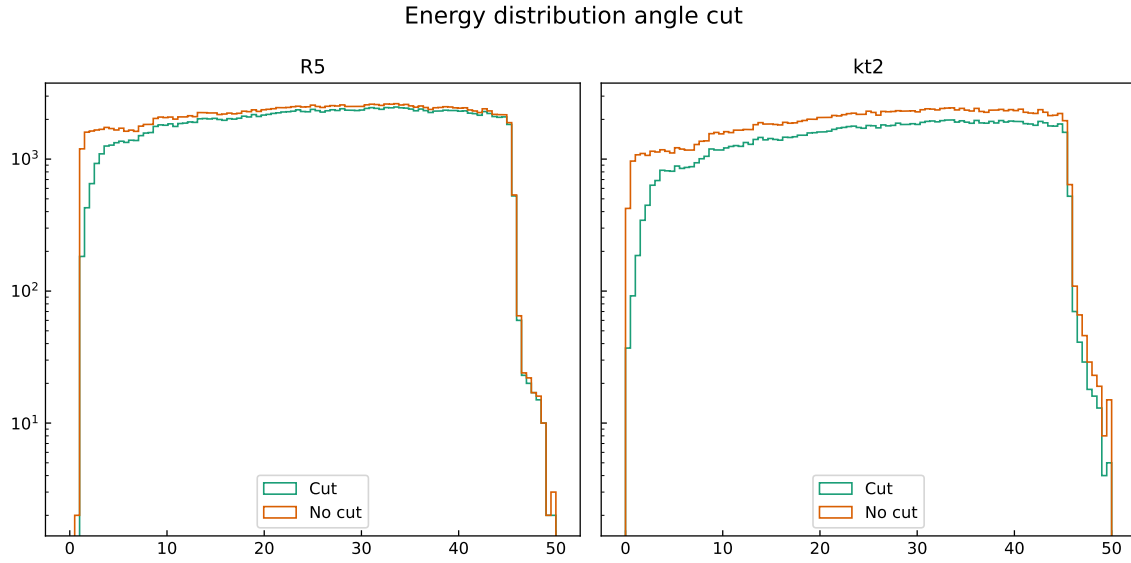


**Figure C.2.:** Jet energy distributions for the explicit reconstruction of the  $Z \rightarrow \tau\tau$  decay. Comparison with and without the jet angle cut.

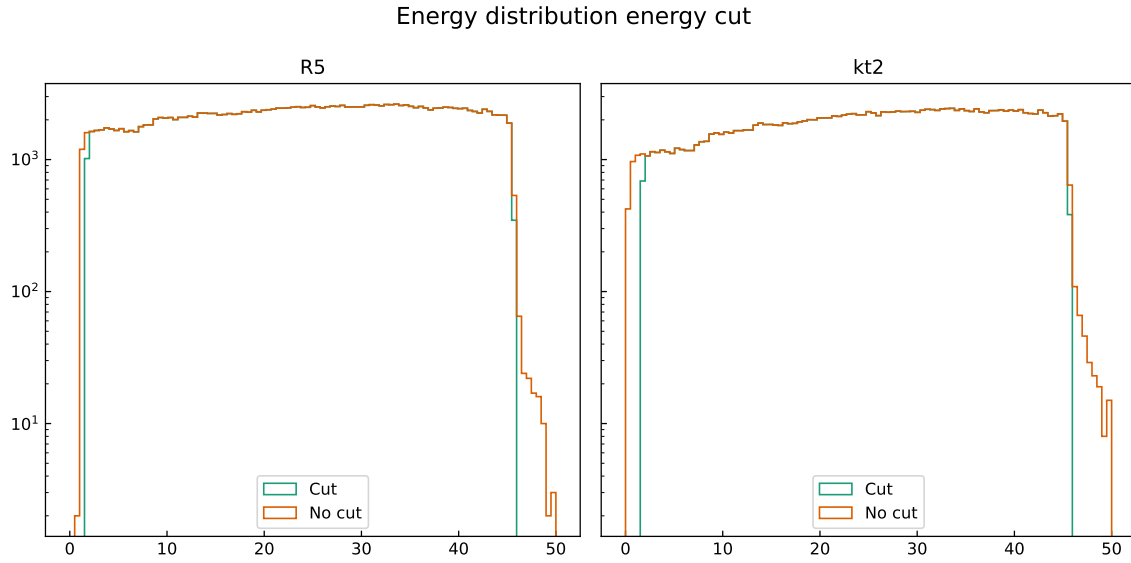


**Figure C.3.:** Jet energy distributions for the explicit reconstruction of the  $Z \rightarrow \tau\tau$  decay. Comparison with and without the jet energy cut.

### C.3. Distribution of the Reconstructed $\pi^0$ Candidate Mass

Using the  $\pi^0$  reconstruction from subsection 4.2.1, candidates for  $\pi^0$  mesons are reconstructed with photons above 200 MeV. Data from  $Z \rightarrow \tau\tau$  and  $Z \rightarrow qq$  are analyzed with

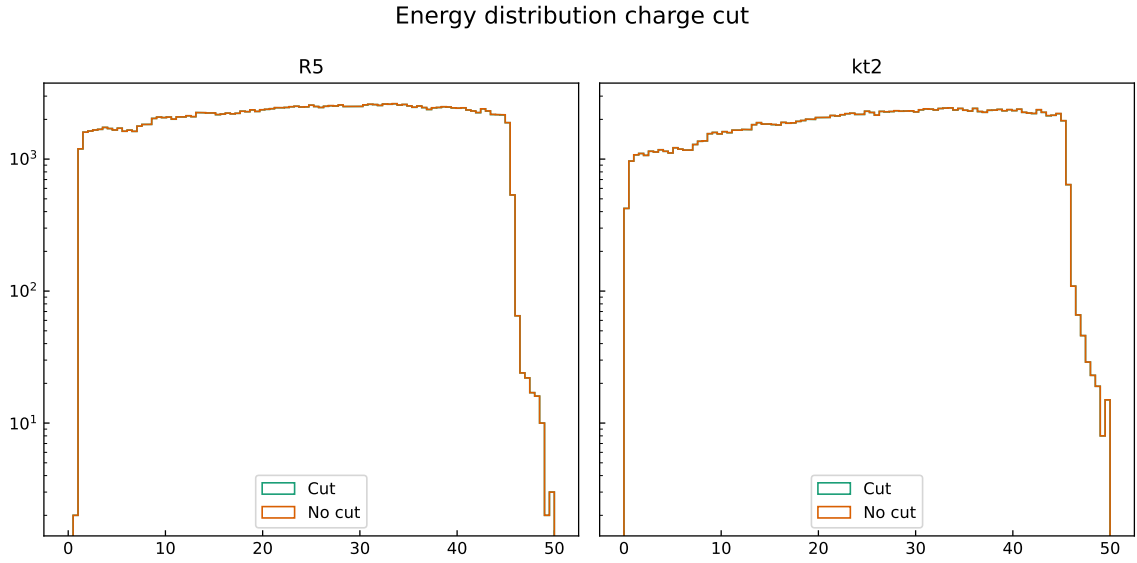


**Figure C.4.:** Jet energy distributions for the explicit reconstruction of the  $Z \rightarrow \tau\tau$  decay. Comparison with and without the jet charge cut.

R5 jet clustering. The function

$$p = \frac{k}{(x - M)^2 + \frac{\Gamma^2}{4}} \quad (\text{C.1})$$

is fitted to the reconstructed  $\pi^0$  mass distribution, with  $M$  and  $\Gamma$  as the mass and width of the  $\pi^0$ , and  $k$  as a scaling factor. The fit, shown in Figure C.5, yields

- $M = (0.135\,125\,7 \pm 0.000\,006\,0) \text{ GeV}$
- $\Gamma = (0.015\,732 \pm 0.000\,013) \text{ GeV}$
- $k = 0.002\,614\,6 \pm 0.000\,002\,7$ .

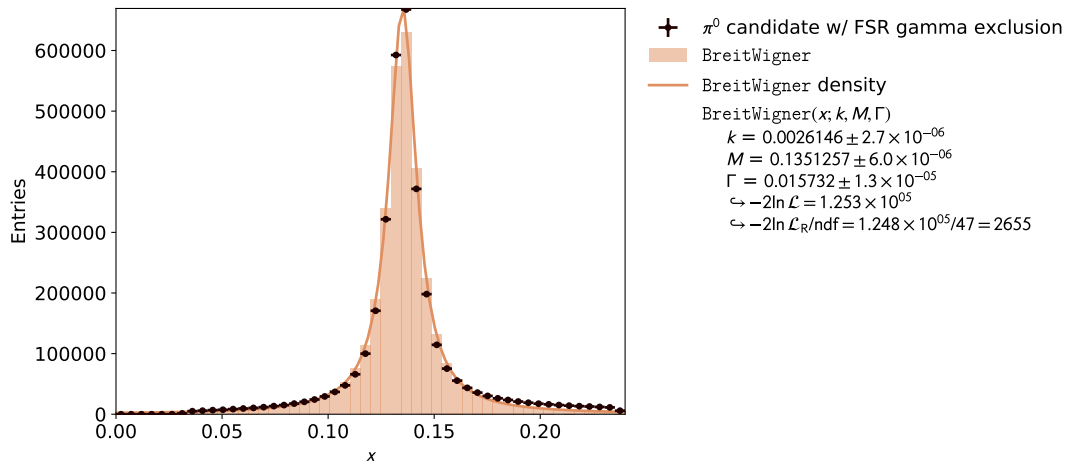


**Figure C.5.:** Distribution of the reconstructed  $\pi^0$  candidate mass for the explicit reconstruction of the  $Z \rightarrow xx$  decays. On the distribution a Breit-Wigner fit is applied.